

Spectroscopic FIR mapping of the disk and galactic wind of M 82 with *Herschel*-PACS^{★,★★}

A. Contursi¹, A. Poglitsch¹, J. Grácia Carpio¹, S. Veilleux², E. Sturm¹, J. Fischer³, A. Verma⁴, S. Hailey-Dunsheath¹,
D. Lutz¹, R. Davies¹, E. González-Alfonso⁵, A. Sternberg⁶, R. Genzel¹, and L. Tacconi¹

¹ Max-Planck-Institut für extraterrestrische Physik, Postfach 1312, 85741 Garching, Germany
e-mail: contursi@mpe.mpg.de

² Department of Astronomy, University of Maryland, College Park, MD 20742-2421, USA

³ Naval Research Laboratory, Remote Sensing Division, 4555 Overlook Ave SW, Washington, DC 20375, USA

⁴ Oxford University, Dept. of Astrophysics, Oxford OX1 3RH, UK

⁵ Universidad de Alcalá de Henares, Departamento de Física, Campus Universitario, 28871 Alcalá de Henares, Madrid, Spain

⁶ Tel Aviv University, Sackler School of Physics & Astronomy, Ramat Aviv 69978, Israel

Received 13 March 2012 / Accepted 5 October 2012

ABSTRACT

Context. We present maps of the main cooling lines of the neutral atomic gas ([OI] at 63 and 145 μm and [CII] at 158 μm) and in the [OIII] 88 μm line of the starburst galaxy M 82, carried out with the PACS spectrometer on board the *Herschel* satellite.

Aims. Our aim is to study the nature of the neutral atomic gas of M 82 and to compare this gas with the molecular and ionized gas in the M 82 disk and outflow.

Methods. By applying PDR modeling we were able to derive maps of the main ISM physical parameters, including the optical depth ($\tau_{\text{[CII]}}$), at unprecedented spatial resolution (~ 300 pc).

Results. We can clearly kinematically separate the disk from the outflow in all lines. The $\tau_{\text{[CII]}}$ is less than 1 everywhere, is lower in the outflow than in the disk, and within the disk is lower in the starburst region.

The [CII] and [OI] distributions are consistent with PDR emission both in the disk and in the outflow. Surprisingly, in the outflow, the atomic and the ionized gas traced by the [OIII] line both have a deprojected velocity of ~ 75 km s⁻¹, very similar to the average velocity of the outflowing cold molecular gas (~ 100 km s⁻¹) and several times smaller than the outflowing material detected in H α (~ 600 km s⁻¹). This suggests that the cold molecular and neutral atomic gas and the ionized gas traced by the [OIII] 88 μm line are dynamically coupled to each other but decoupled from the H α emitting gas.

Conclusions. We propose a scenario where cold clouds from the disk are entrained into the outflow by the winds where they likely evaporate, surviving as small, fairly dense cloudlets ($n_{\text{H}} \sim 500\text{--}1000$ cm⁻³, $G_0 \sim 500\text{--}1000$, $T_{\text{gas}} \sim 300$ K). We show that the UV photons provided by the starburst are sufficient to excite the PDR shells around the molecular cores and probably also the ionized gas that flows at the same PDR velocity. The mass of the neutral atomic component in the outflow is $\geq 2\text{--}8 \times 10^7 M_{\odot}$ to be compared with that of the molecular component ($3.3 \times 10^8 M_{\odot}$) and of the H α emitting gas ($5.8 \times 10^6 M_{\odot}$). The mass loading factor, $\dot{M}_{\text{outflow}}/SFR$, of the molecular plus neutral atomic gas in the outflow is ~ 2 . Energy and momentum driven outflow models can explain the data equally well, if all the outflowing gas components are taken into account.

Key words. galaxies: individual: M 82 – infrared: ISM – galaxies: kinematics and dynamics – galaxies: starburst

1. Introduction

In the last decades, the primary role of galactic outflows on galaxy evolution has become evident (Heckman et al. 1990; McKeith et al. 1995; Lehnert & Heckman 1995; Heckman 1998; Veilleux et al. 2005; Springel et al. 2005). Outflows in galaxies powered by either active galactic nuclei (AGNs) or starbursts have been introduced in theoretical models (e.g. Croton et al. 2006) as sources of negative feedback, that terminate black-hole growth and/or star-formation and to explain the tight correlation between the mass of the black hole, and the velocity dispersion or mass of the bulge in which it resides (Magorrian et al. 1998; Gebhardt et al. 2000; Merritt & Ferrarese 2001; Tremaine et al. 2002; Gültekin et al. 2009). These outflows contain a hot

(10^7 K) metal-enriched wind, in addition to entrained cooler gas and dust. Therefore, they may significantly influence the chemical evolution of both the interstellar medium (ISM) of the galaxy and the intergalactic medium (IGM) where this processed material might be eventually dispersed.

Nearly all galaxies with high star formation rates show signs of outflows (Rupke et al. 2005a–c). They also seem to be ubiquitous in Lyman break galaxies at $z \sim 3$ where they are capable of creating holes of ~ 100 kpc in the surrounding IGM (Pettini et al. 2001; Shapley et al. 2003; Steidel et al. 2010; Genzel et al. 2010), in Lyman- α emitting galaxies at $z \sim 4$ (Finkelstein et al. 2011) and compact gas rich damped Lyman- α at $z = 2.2$ (Noterdaeme et al. 2012). Recently, very massive molecular and neutral gas AGN-driven outflows have been discovered in Mrk 231 (Fischer et al. 2010; Feruglio et al. 2010; Rupke & Veilleux 2011; Ciccone et al. 2012), in the local early type galaxy NGC 1266 (Aalto et al. 2011), in a $z = 2$ quasi-stellar object (QSO; Weiß et al. 2012) and in others ultra-luminous infrared galaxies (ULIRGs; Sturm et al. 2011; Chung et al. 2011).

* Appendix A is only available in electronic form at <http://www.aanda.org>

** The reduced data (FITS files) are only available at the CDS via anonymous ftp to cdsarc.u-strasbg.fr (130.79.128.5) or via <http://cdsarc.u-strasbg.fr/viz-bin/qcat?J/A+A/549/A118>

Sturm et al. (2011) provided the first observational evidence that molecular outflows in some ULIRGs are powered by the AGN and that the mass outflow rates of the outflowing material exceed the star formation rate (SFR) of the host galaxies, confirming the theoretically postulated fundamental role of the outflows on galaxy evolution.

The evident cosmological importance of this phenomenon has brought many astronomers to study a few nearby galactic winds in great detail. M82 is the best studied case. It is the closest (at a distance of 3.6 Mpc, Freedman et al. 1994) and the brightest galaxy hosting a spectacular bipolar outflow along its minor axis, although not as massive and energetic as those recently discovered in ULIRGs. Nevertheless, thanks to its proximity and to its favorable disk inclination ($i = 81^\circ$), M82 is one of the nearby galaxies most studied at all wavelengths and has therefore become the archetype of a starburst with an outflow, with no AGN.

M82 has undergone two powerful starburst episodes located in the central ~ 500 pc of the galaxy. The first starburst was triggered 10^7 yr ago by the encounter with M81, 10^8 yr ago. The second starburst was most likely bar driven 5×10^6 yr ago (Förster Schreiber et al. 2003). Both of these starbursts comprise several star clusters each hosting many hundreds of young massive stars (Melo et al. 2005). The superwind which feeds the bipolar outflow along the minor axis of the galaxy is generated in the inner 350 pc of the galaxy where intense diffuse hard X-ray emission is detected (Strickland & Heckman 2007). The outflow reveals filamentary structures at many wavelengths: they are well visible in any high spatial resolution observation such as in the optical H α , [NII] and [OIII] lines (Shoppell & Bland-Hawthorn 1998), Xray (Strickland & Heckman 2007), warm molecular hydrogen (Veilleux et al. 2009) and PAHs (Engelbracht et al. 2006). Simulation of galactic winds generated by starburst show that these filamentary structures originate from the fragmentation of clouds stripped from the disk and accelerated by the ram pressure in the wind (Cooper et al. 2008). Cold and warm dust and molecular gas are found in a biconical-like structure extending up to 3 kpc away from the stellar disk on both sides, as revealed by UV scattered light (Hoopes et al. 2005), PAH emission (Engelbracht et al. 2006; Kaneda et al. 2010) sub-millimeter continuum emission (Leeuw & Robson 2009; Roussel et al. 2010), ^{12}CO ($J 1 \rightarrow 0$) (Walter et al. 2002; Weiß et al. 2005), ^{12}CO ($J 3 \rightarrow 2$) (Sequist & Clark 2001) line emission and H $_2$ near infrared observations (Veilleux et al. 2009). Most likely, this material has been entrained by the wind. Further out, most of the dust (Roussel et al. 2010) and gas (Yun et al. 1994) associated with the halo seems to originate from the tidal interaction with M81.

The bipolar outflow shows different morphologies in the north and in the south, especially at optical wavelengths (Shoppell & Bland-Hawthorn 1998; Westmoquette et al. 2009a,b; Sequist & Clark 2001). The southern wind is approaching us and is more clearly visible because the inclination of M82's disk provides a more direct sight-line to the southern part of the disk. The northern outflow is receding from us and is likely to be more heavily obscured by the disk itself. This is why most detailed studies of M82's outflow have focused on the southern rather than the northern outflow of M82 (Westmoquette et al. 2009a,b; Shoppell & Bland-Hawthorn 1998).

The most accepted interpretation of the outflowing material in M82 is the following: the supernova explosions and stellar winds of the starburst blow away a collimated hot ($\sim 10^8$ K) gas, detected in the center of the galaxy in X-ray

(Griffiths et al. 2000). The wind also drags cold material from the disk into the outflow. The collision between the hot fluid and the entrained cold clouds produces X-ray emission further out along the outflow. These clouds are heated by shocks and the UV radiation from the starburst producing most of the H α emission. The cold material in the winds has been observed in its dust and molecular component and is directly illuminated by the light of the starburst for at least ~ 1 kpc in both directions (Veilleux et al. 2009).

So far little observations are available on the neutral atomic component of the outflow. Observations in the HI line of the M81/M82 group revealed many tidal streams from M82 (Yun et al. 1994; Chynoweth et al. 2008), but no detailed study has been conducted on the HI associated with the winds. Colbert et al. (1999) have studied the far infrared (FIR) fine structure lines observed with the LWS instrument on board of the Infrared Space Observatory (ISO) but the spatial ($\sim 80''$) and spectral ($\sim 10^3$ km s $^{-1}$) resolution were too poor to distinguish the outflow and the disk components. This is why we observed M82 with the PACS spectrometer (Poglitsch et al. 2010) on board of the *Herschel* satellite (Pilbratt et al. 2010) in the [OI] lines at 63.2 and 145.6 μm , and the [NII], [CII] and [OIII] lines at 121.89, 157.7 and 88.3 μm respectively, as part of the SHINING guaranteed time key project (P.I. E. Sturm). With these observations we were able to resolve for the first time *both spatially and kinematically* the disk and the outflow of M82 in the main FIR fine structure lines.

This paper is organized as follows: details on the observations and data reduction are given in Sect. 2. The resulting maps and related uncertainties are presented in Sect. 3. In Sect. 4 we explain the Photodissociated regions modeling of our observations and we discuss the meaning of the physical parameters resulting from this modeling. We also compare the various gas phases participating to the outflow and we discuss their energetics and their relation. In Sect. 5 we summarize the main conclusions.

2. PACS spectrometer observations and data reduction

We have observed M82 with a 5×5 (4×4) raster in the blue (red) channel, and with step sizes in YZ spacecraft coordinates equal to: $step_z = 16.0''$ ($24.0''$) and $step_y = 14.5''$ ($22.0''$), in bright line scan chopped mode, with large chopper throw in the following fine structure lines: [OI] ($^3P_2 \rightarrow ^3P_1$) and ($^3P_1 \rightarrow ^3P_0$) lines at 63.2 and 145.6 μm , [CII] ($^2P_{1/2} \rightarrow ^3P_{3/2}$) line at 157.7 μm and [OIII] ($^3P_0 \rightarrow ^3P_1$) line at 88.3 μm . The on source integration times per raster position are: ~ 40 , 40, 65, and 33 s for the [OI] 63, [OIII] 88, [OI] 145 and [CII] 158 lines respectively. Although the bright line mode executes less grating steps *per scan* than the *faint mode*, it nevertheless attains Nyquist sampling. The spectral resolutions for the lines are: ~ 3300 (87 km s $^{-1}$), ~ 2400 (125 km s $^{-1}$), 1160 (257 km s $^{-1}$) and ~ 1255 (240 km s $^{-1}$), respectively.

The spatial steps used in the rasters, in combination with the spaxel pattern of the instrument, ensure spatially Nyquist sampled final maps.

For each line, each raster position has been reduced in HIPE¹ with the standard pipeline up to the rebinnedCube task. Then, a polynomial continuum plus a Gaussian profile in each pixel

¹ HIPE is a joint development by the *Herschel* Science Ground Segment Consortium, consisting of ESA, the NASA *Herschel* Science Center, and the HIFI, PACS and SPIRE consortia.

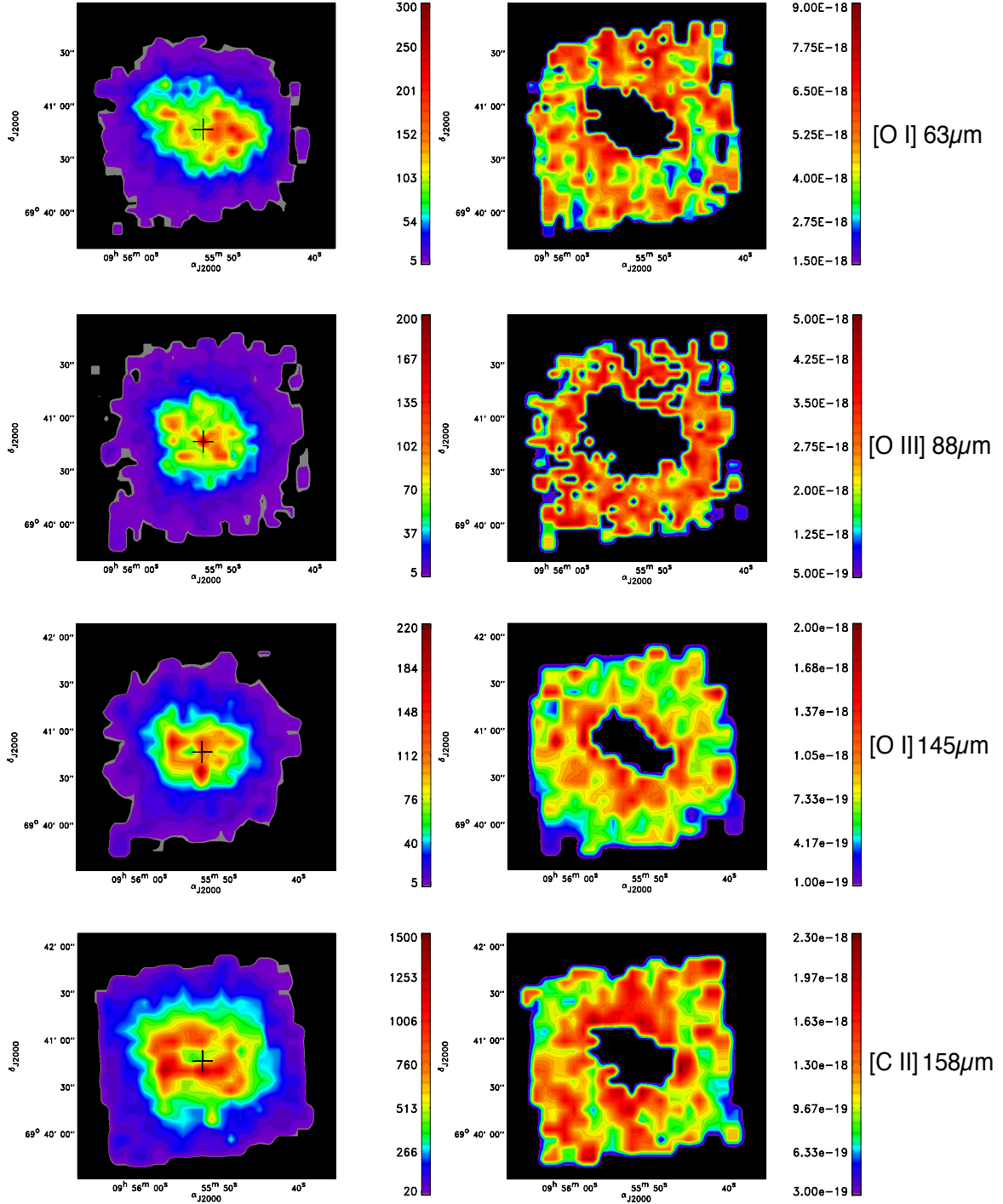


Fig. 1. *Left column:* for each line the signal to noise ratios maps. *Right column:* for each line the “error” maps in W m^{-2} , obtained as explained in Sect. 2 with the central region masked. (This figure is available in color in the electronic form.)

at each raster position have been fitted, and the corresponding intensity, wavelength peak, full width at half maximum (FWHM) and celestial coordinates were recorded. In an external package we built the final maps applying the drizzle algorithm (Fruchter & Hook 2002). Thus, we produced intensity, peak velocity and line width maps for the four observed lines. Moreover, thanks to the brightness of M 82 we were also able to produce high spatial resolution continuum maps using the continuum measured from our line observations as well as from the data in the parallel channels. The final maps cover the disk and the base of the outflow of M 82 up to 1 kpc away from the disk in

both direction, at an unprecedented spatial resolution (from 130 to 270 pc) and sensitivity (see Fig. 12 of Poglitsch et al. 2010) at these wavelengths. Taking into account pointing offset and jittering during observations and the uncertainties related to the fact that we arbitrarily assign the coordinates at the center rather than at the corner of the final pixel, we estimate an overall astrometric uncertainty of $\sim 4''$.

In addition to the rasters, we have observed M 82 also in the ($^3\text{P}_1 \rightarrow ^3\text{P}_2$) [NII] line at 121.89 μ m in faint chop-nod line scan mode, with 3 separate staring observations pointed on the galaxy’s center, the northern and the southern outflow. These

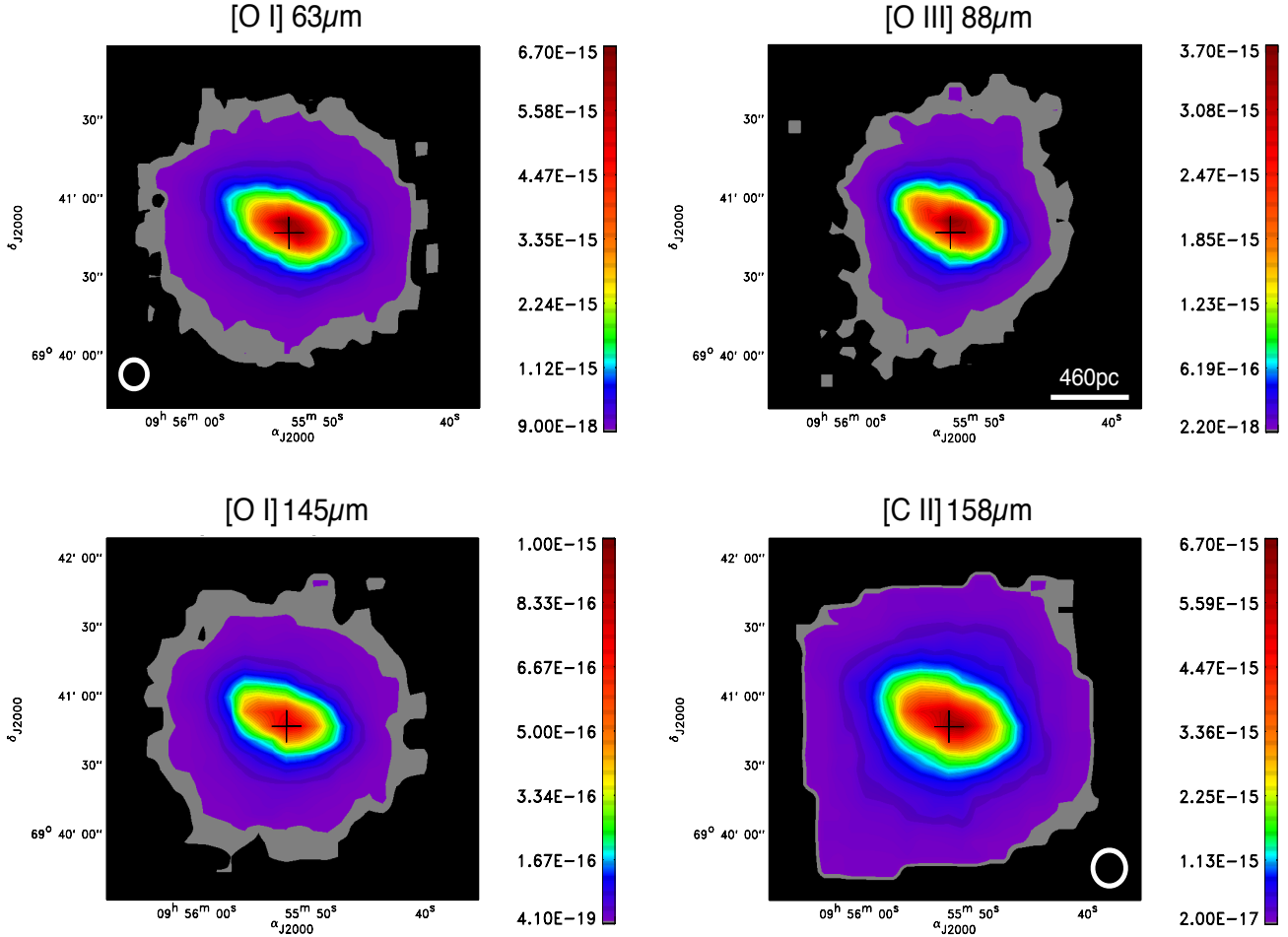


Fig. 2. Integrated line emission of the 4 observed lines at their original spatial resolution. Typical PSF widths are shown for the shortest and longest wavelengths. Units are in W m^{-2} . The black cross corresponds to the adopted center of M 82, i.e. $9^{\text{h}}55^{\text{m}}52.2^{\text{s}}$ $69^{\text{d}}40^{\text{m}}46.6^{\text{s}}$ (J2000) (Dietz et al. 1986). North is up and East is towards the left. (This figure is available in color in the electronic form.)

data were reduced in HIPE up to the rebinned cube step resulting in 25 line intensity values per pointing.

For each of the fitted spectra we have estimated the errors from the residual spectrum, i.e. the original spectrum minus the fitted continuum plus Gaussian profile. These errors contain the noise of the spectrum as well as systematic deviations from a perfect fit. These errors were quoted in the same units as the fitted line fluxes, i.e., W m^{-2} per each spaxel. The line flux error maps were generated with exactly the same drizzle scheme as for the line map. In order to create the error maps by the same method as for the flux, we used the intermediate quantity $1/\text{errors}^2$ which can be drizzled as an extensive variable. However, caution must be taken when interpreting the resulting errors for the following reasons. In principle, if we were dealing with statistical noise only, by observing the same spot in the sky several times, as we effectively do when we combine different rasters in the drizzle, the error of the combined measurements would go down. If there is a systematic error it will always be the same in sign and magnitude and will not cancel with repeated measurements. Furthermore, the errors in the regions where the error/signal ratio is better than the calibration accuracy (explained in detailed in Sect. 3.4) should not be quoted as absolute measurement errors. This explains why we have an increase of the estimated “errors” where the signal is stronger. Therefore, these maps are meaningful only in the “outskirts” of the galaxy but not in the starburst region and for this reason we

masked the starburst regions in the “error” maps shown in the right column of Fig. 1. In order to give a complete picture of the final “noise” levels we reach in each map, we show in Fig. 1 also the S/N maps.

3. Results

3.1. FIR line intensity and continuum maps

Figure 2 shows the line intensity maps of the 4 lines in their original spatial resolution. All maps are north-south oriented. The crosses represent the center of M 82. The brightest integrated line emissions are very similar at all wavelengths but at the faint emission level, some important differences are noticeable. The two lines tracing exclusively the neutral atomic gas, namely [OI] $63 \mu\text{m}$ and [OI] $145 \mu\text{m}$, show a spherical morphology, while the [CII] emission, that arises mainly in the neutral atomic medium but also from the ionized medium, shows a weak elongation towards the minor axis. This elongation becomes more evident in the [OIII] $88 \mu\text{m}$ line intensity maps, that traces purely ionized gas. In all maps, emission up to 1 kpc on both sides of the disk along the minor axis is detected. From these maps it is evident that the ionized medium has an emission elongated along the minor axis of the galaxy while the emission arising from the neutral medium is more spherically distributed, although still detected along the minor axis of the galaxy.

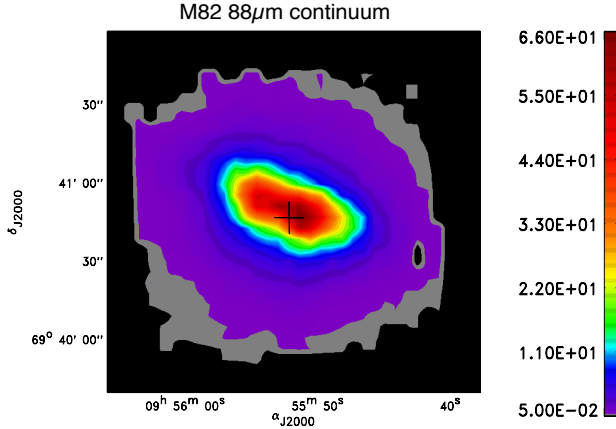


Fig. 3. Offline continuum emission obtained from the continuum in the [OIII] 88 μm line. Units are in Jy. The black cross corresponds to the adopted center of M 82. (This figure is available in color in the electronic form.)

Figure 3 shows the continuum map derived from the observation of the [OIII] 88 μm emission line. The continuum maps at the other wavelengths show a similar morphology and therefore they are not shown here. The continuum morphology is spherical and, at the faint level of the emission, does not show a marked asymmetry along the galaxy’s minor axis. The brightest continuum emission region is displaced $\sim 6''$ west with respect to the center of the galaxy (black cross in the figure). This is marginally larger than the final astrometric uncertainties of our maps ($\sim 4''$). The peak emission moves towards the east with increasing wavelengths indicating that the western part is hotter than the eastern part in the starburst region of M 82.

3.2. Velocity dispersion maps

Figure 4 shows the velocity dispersion maps obtained from FWHM of the line fits, converted in velocity and corrected for the instrumental profile. The overall shape is similar in all lines and it is formed by two well distinct kinematic structures: the disk and the outflow. In general the two cones of the outflow have a velocity dispersion higher (from ~ 50 to ~ 100 km s^{-1} or a factor from 1.5 to 2) than the disk.

All four maps clearly show emission in the outflow aligned along the minor axis. This enhanced emission originates from a point that coincides with the center of the disk (as marked by the black cross in the figure). The yellow ellipse shown in the figure corresponds to the stellar disk defined by the emission in the K_s -band, as shown in Fig. 9 and explained in Sect. 3.5.

3.3. Radial velocity maps

Figure 5 shows the radial velocity maps, obtained from the wavelength corresponding to the fitted lines peak converted into velocity, from which we have subtracted the systemic velocity of M 82 equal to 203 km s^{-1} (Shopbell & Bland-Hawthorn 1998). The overall S-shape morphology of the velocity field is similar in all lines and confirms previous findings: the east part of the disk and the north outflow are receding from us while the west part of the disk and the southern outflow are approaching us. The region where the velocity is zero is consistent in all 4 maps and it corresponds to the galaxy’s center (black crosses). The velocity in the disk goes from ~ -80 to 100 km s^{-1} in all lines but the [OI] 145 μm line, which is shifted by $\sim +20$ km s^{-1} with respect

to the others. This shift is present in all raster positions suggesting a systematic error (see next section for details) rather than a real physical effect. We have also derived rotation curves along the major axis of the galaxy (see Fig. 6). All curves are consistent with each other (except for the velocity shift in the rotation curve obtained with the [OI] 145 μm line) and they also agree with those shown by Shopbell & Bland-Hawthorn (1998), especially with those in $H\alpha$ and $^{12}\text{CO}(J_2 \rightarrow 1)$.

It is important to note that *we do not detect line splitting in any of the observed lines*. This is particularly intriguing for the [OIII] line at 88 μm . Indeed, line splitting is clearly detected in $H\alpha$ in the outflow, above 300 pc from the galaxy plane along the minor axis of the galaxy, with velocity separation of ~ 200 km s^{-1} (Greve et al. 2004), well above the PACS spectral resolution of the [OIII] line at 88 μm (120 km s^{-1}). It is not clear whether line splitting is detected in the optical [OIII] lines: Shopbell & Bland-Hawthorn (1998) report marginally detected [O III] 5007 \AA line splitting in some regions of the mapped area but the low S/N prevented them to fit double Gaussians to their [O III] 5007 \AA data and therefore to be more quantitative on this issue. As will be discussed later, this is not the only striking difference we find between the gas emitting in the [OIII] line at 88 μm and that emitting in $H\alpha$.

From the [OIII]/[OI] 63 μm map we will present in Sect. 3.5, where the bipolar outflow can be best determined, we measure an opening angle of $\sim 50^\circ$ for both sides of the outflow, very similar to the value found by Walter et al. (2002) in the CO maps. Taking into account the disk inclination of M 82 ($i = 81$), the outflow opening angle, and assuming a simple jet-like geometry, we can derive the mean de-projected velocity dividing the observed velocity (~ 40 – 45 km s^{-1}) by $\sin(81^\circ - 50^\circ/2)$. This results in a mean deprojected velocity from ~ 75 to 85 km s^{-1} , similar within the wavelength uncertainties, in both cones of the outflow and at both wavelengths, i.e. for both the ionized gas traced by the [OIII] emission and the neutral gas traced by the two [OI] lines and the [CII] line.

3.4. Uncertainties

The dominant source of *flux uncertainties* in our data are those related to the spectrometer flux calibration, that is $\sim 30\%$ in both the blue and the red channels (Poglitsch et al. 2010). In the raster observations presented here, another source of error arises from the fact that for all observed lines we used the *bright line* mode, i.e. less grating steps per grating scan than in faint line mode. The reason for having chosen this observing mode is that these maps were executed during the performance verification phase, to check that the PSF sampling scheme for the mapping mode worked as expected. In order to test it we had to observe as many wavelengths as possible along the full PACS wavelength range (55 – 220 μm), and faint line mode would have taken a prohibitive amount of time.

In bright line mode each of the 16 spectral pixels of one spatial pixel (hereafter spaxel) does not see the full line, as in the case of faint line-scan. As a consequence, one of the crucial steps of the faint line mode data reduction, bringing the response of the 16 spectral pixels of each spaxel to the same continuum level (the so called FlatField task) cannot be applied in the case of bright line mode. Figure 7 shows an example of a spectrum before rebinning and combining the nodes, for the central spaxel of the central raster position at 63 μm . Each spectral pixel of the central spaxel has a different color. The figure clearly shows how small is the overlapping spectral range seen by subsequent

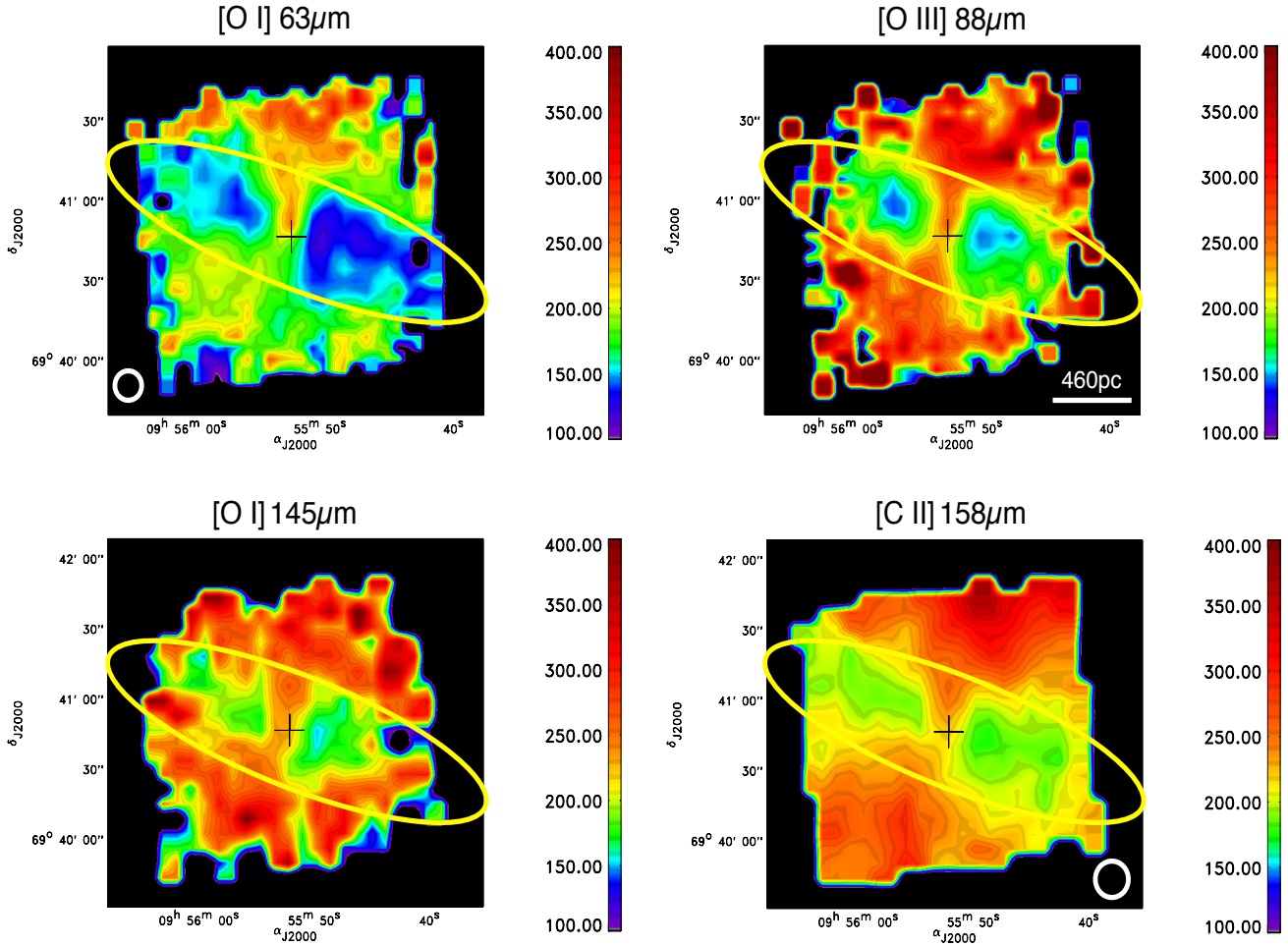


Fig. 4. Velocity dispersion maps obtained from the fitted line widths deconvolved with the instrumental profile width, in km s^{-1} . The black cross corresponds to the adopted center of M82. The yellow ellipse corresponds to the stellar disk as described by the K_s -band emission shown in contours in Fig. 9. (This figure is available in color in the electronic form.)

spectral pixels of each spaxel and illustrates the difficulties in flat fielding this type of observations. The lack of the flat field could result in distorted line profiles, and therefore it could affect the velocity peak, the FWHM and the total flux.

To evaluate the impact of this particular observing mode on the intensity maps, we have compared the LWS line flux of M82 given in Brauher et al. (2008) and by Colbert et al. (1999) with ours. We have assumed a circular Gaussian LWS beam profile, with a FWHM equal to $80''$ at all wavelengths but at $158 \mu\text{m}$ where we assumed a FWHM equal to $70''$ (Lloyd 2003). We integrated the line and continuum PACS flux under the assumed LWS profiles and we compared the obtained fluxes with those observed with LWS corrected for the LWS extended source correction factor (see Table 7 of Brauher et al. 2008). The results are shown in Fig. 8. The LWS and PACS fluxes do agree within the respective uncertainties adopted equal to 30% for PACS and 20% for LWS as claimed in Brauher et al. (2008), with the possible exception of the continuum flux density at $88 \mu\text{m}$ which only marginally agrees with the adopted uncertainties. We conclude that the bright line mode does not introduce uncertainties greater than the nominal PACS spectrometer flux uncertainties.

The nominal uncertainties due to the *wavelength calibration* are $\sim 20 \text{ km s}^{-1}$ and $\sim 40 \text{ km s}^{-1}$ in the blue and red channel respectively (Poglitsch et al. 2010). A distortion of the line profile due to the bright line mode could introduce further uncertainties which is difficult to quantify. However, we expect these

uncertainties to increase with decreasing line intensity where the distortion of the lines profiles become more significant. Among the four observed lines, the [OI] $145 \mu\text{m}$ line is by far the weakest. Therefore, we expect the velocity line peak of this line to be more affected than the others due to this observing mode. This could in principle explain the shift observed in the rotation curve of this line with respect to the rotation curves obtained in the other lines and visible in the mono dimensional rotation curves shown in Fig. 6. On the other hand, the issues with the bright-line mode would modify the line profiles in a random way, because the misalignment of the spectrum among the spectral pixels of the same spaxel depends on the transient history of each pixel and on the mispointing, which has no systematic direction. Since the observed shift in the [OI] $145 \mu\text{m}$ line is systematic in all the raster positions, we believe that the problem arises from a wavelength calibration issue at this wavelength. We note however, that the fact that the rotation curves in the other lines agree with those previously published indicates that the bright line mode does not introduce significant additional uncertainties even at $145 \mu\text{m}$ and that the data are dominated by the nominal wavelength calibration uncertainties.

The deformation of the line-shape due to the bright line mode is also a random process and it would affect the fitted FWHM from which we have derived the velocity dispersion maps shown in Fig. 4. The fact that all maps show the same kinematic morphology, ensures that the line deformation does not affect the

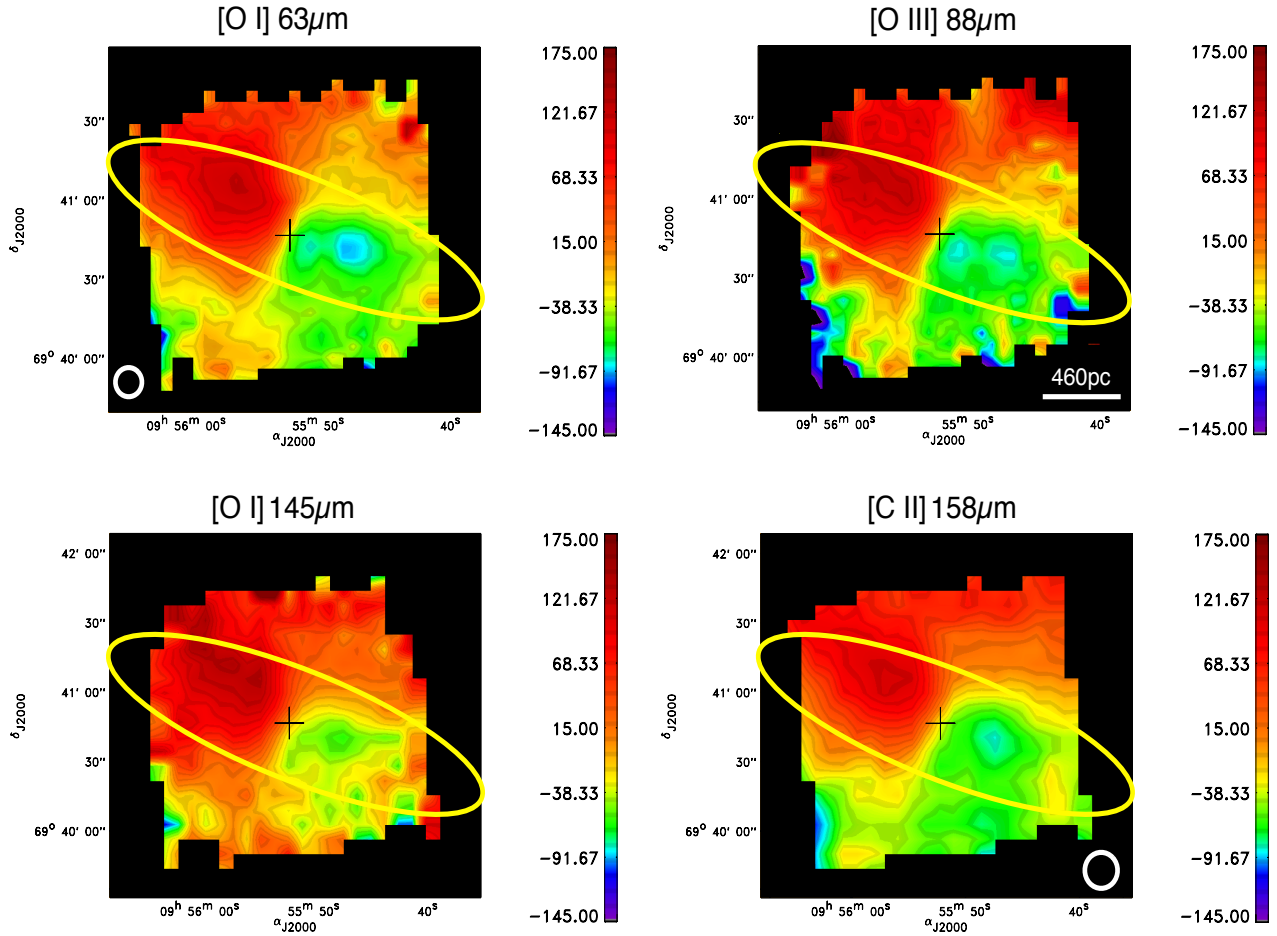


Fig. 5. Radial velocity maps obtained from the fitted line profiles at each position. The black cross corresponds to the adopted center of M 82. (This figure is available in color in the electronic form.)

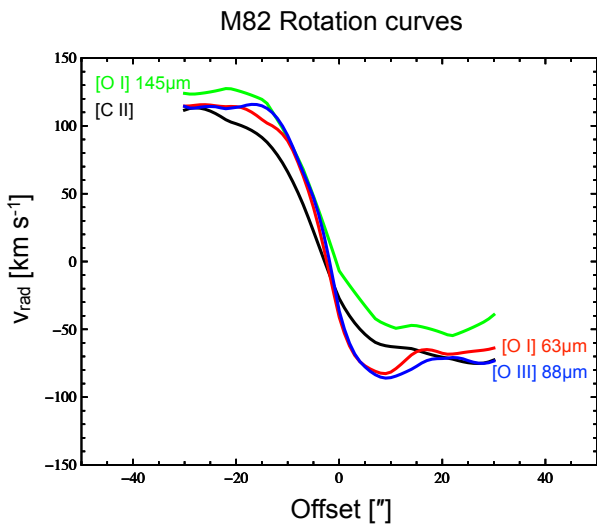


Fig. 6. Rotation curves along the major axis of M 82 in the 4 observed lines. Note the shift of the rotation curve obtained in the [O I] 145 μm line which is not a real physical effect (see Sect. 3.4 for details). (This figure is available in color in the electronic form.)

overall velocity dispersion in a systematic way, producing fake structures.

3.5. Ratio maps

Figure 9 shows the [OI] 63 μm /[CII], [OIII]/[OI] 63 μm , [OIII]/[CII] and [OI] 145 μm / [OI] 63 μm ratio maps. Before making each ratio map, the two images have been smoothed to the same resolution, if necessary. The HST $H\alpha$ contours (Mutchler et al. 2007) are overplotted on the [OIII]/[OI] 63 μm ratio map (see discussion in the next section).

The ratio maps are very different from each other: the [OI] 63 μm /[CII] shows an overall asymmetry along the disk major axis, while in the [OIII]/[OI] 63 μm map and, at a poorer resolution also in the [OIII]/[CII] ratio map, the bipolar outflow is very clearly delineated. On the [OI] 63 μm /[CII] ratio map in Fig. 9, the K_s -band contours (Veilleux et al. 2009) describing the stellar disk are also plotted. Based on these contours we have defined two ellipses: one external (yellow in Fig. 9) describing the overall stellar disk and one internal (purple in Fig. 9) that defines the brightest part of the stellar disk including the starburst region.

While the region where the [OI] 63 μm / [CII] ratio is high corresponds well to this internal ellipse, the region where the [OIII]/[OI] 63 μm ratio is higher arises from the north part of the starburst region. A comparison with the $^{12}\text{CO}(J 1 \rightarrow 0)$ map (Fig. 1 of Weiß et al. 2005) with the [OIII]/[OI] 63 μm ratio image shows that the outflow coincides with the regions marked as outflow in their figure. The northern outflow is a factor of ~ 2 brighter in the [OIII]/[OI] 63 μm ratio than the

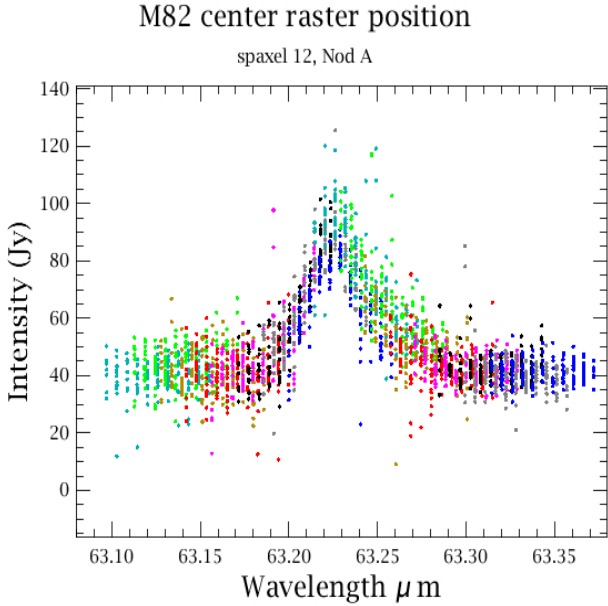


Fig. 7. Example of bright line mode observation. The figure shows the spectrum of all spectral pixel of the central spaxel of the field of view, in different color for each spectral pixel, for Nod A. (This figure is available in color in the electronic form.)

southern one. In contrast, at optical wavelengths the northern outflow has not been detected in the [OIII] emission line at 5007 Å while the southern outflow is clearly visible at this wavelength (Fig. 2 of Shopbell & Bland-Hawthorn 1998). It seems unlikely that the difference in the observed [OIII] 5007 Å line emission in the two cones of the outflow of M 82 is due to an electron density higher than the critical density of the [OIII] line at 5007 Å ($6.3 \times 10^5 \text{ cm}^{-3}$) in the northern outflow. In fact, the estimated averaged electron density in the outflow is $\lesssim 300 \text{ cm}^{-3}$ (Yoshida et al. 2011), and the average electron density associated with the filaments emitting in H α is $\sim 15 \text{ cm}^{-3}$ (Shopbell & Bland-Hawthorn 1998). As we will argue in the next section, we believe that this difference can be explained with the extinction being higher in the northern than in the southern outflow.

The [OI] 145/[OI] 63 μm ratio is shown in Fig. 9. This ratio varies only by a factor of 2 all over the mapped area, and neither the outflow nor the stellar disk are clearly visible. In the starburst region defined by the purple ellipse, this ratio appears slightly weaker than elsewhere. Figure 2 of Tielens & Hollenbach (1985) shows how this ratio depends on the gas temperature for various gas densities. For gas temperatures higher than $\sim 300 \text{ K}$ and a fixed gas density this ratio is basically constant and it decreases with increasing density. The comparison with the range of ratios observed in M 82 ($\sim 0.05\text{--}0.1$) suggests that the gas temperature is greater than $\sim 300 \text{ K}$ everywhere and that the density is higher in the central region where this ratio is lower. We will see in Sect. 4.2 that more detailed modeling confirms that this is the case.

Finally, Fig. 10 shows the line over the continuum as measured around the [OIII] and [OI] 63 μm lines. These figures confirm that both the neutral and the ionized gas traced by the FIR fine structure line participate in the outflow, but that the ionized gas is more collimated than the neutral gas. This fits well in the picture where the cold entrained gas forms an outflow less collimated than the hot gas (Ohyama et al. 2007). However, the ionized gas traced by the [OIII] line at 88 μm is kinematically coupled with the neutral atomic gas and it is not kinematically coupled with the ionized gas traced by the H α emission

(Greve 2004) because it moves at a much lower velocity than the hot (10^4 K) gas.

3.6. Comparison with H α

In order to understand where the outflow outlined in the [OIII]/[OI] 63 μm ratio map is located with respect to the well known bipolar outflow of M 82 observed at other wavelengths, the HST H α contours are overplotted on the [OIII]/[OI] 63 μm ratio map in Fig. 9. Overall, the H α emission is more extended than the [OIII]/[OI] 63 μm ratio (orange contours in the upper right panel of Fig. 9). The bulk of the H α emission, i.e. the “eyes” defined in Shopbell & Bland-Hawthorn (1998) (black contours in the upper right panel of Fig. 9), are displaced with respect to the region with the highest [OIII]/[OI] 63 μm ratio. Actually, the region with the brightest [OIII]/[OI] 63 μm ratio almost envelopes the H α “eyes”. Also, in the northern outflow the H α emission is displaced to the west with respect to the region with the highest [OIII]/[OI] 63 μm ratio, while in the southern outflow both emission are co-spatial. This displacement is most likely due to extinction of the optical emission; in fact, the disk of M 82 is inclined by 81 degree in the sense that its southern part is offered to our direct line of sight. Thus, the emission of the northern part of the disk and part of the northern outflow must suffer from a higher obscuration than that in southern outflow. This agrees very well with what was found by Shopbell & Bland-Hawthorn (1998) who calculated that, given the inclination of M 82 disk, the northern outflow should be at least partially obscured up to a projected radius of $\sim 48''$. This corresponds to the extension of the bright blob visible in the [OIII]/[OI] 63 μm map, north-east from the northern H α emission.

Extinction could also explain the fact that the northern outflow is detected in [OIII] at 88 μm but not at 5007 Å. We tried to make a very rough estimate of the extinction in the following way: we estimated the logarithm of the H α /H β ratios of both sides of the outflow (0.6 and 1.2 for the southern and the northern respectively) at a distance of $\sim 500 \text{ pc}$ from the galaxy center from Fig. 16 of Heckman et al. (1990). With these values, we could calculate the A_V/R_V in the northern and southern outflow using the Calzetti law (Calzetti et al. 1994). We derived a very crude value of the observed [OIII] 5007 Å line flux in the southern outflow from Fig. 2 of Shopbell & Bland-Hawthorn (1998) and, using a slab geometry, the corresponding dereddened flux. Assuming that the intrinsic [OIII] 5007 Å emission in the northern outflow is equal to that of the southern outflow, we estimated the expected flux, using the A_V/R_V values obtained for the northern outflow. We find that the expected [OIII] 5007 Å flux is $\sim 2 \times 10^{-17} \text{ erg s}^{-1} \text{ cm}^{-2}$ for the slab model which is appropriate for the Calzetti law. This flux is smaller than the minimum flux reported by Shopbell & Bland-Hawthorn (1998) in their Fig. 2, and it is compatible with the non-detection of the [OIII] 5007 Å line in the northern outflow. We stress, however, that this calculation is highly uncertain, first, because of the very uncertain input values which we had to deduce from the published figures, second because there is no physical reason to assume that the intrinsic [OIII] 5007 Å emission in the two cones of the outflow should be the same.

One important question is whether in the outflow, the bulk of [OIII] 88 μm line emitting gas is associated with the bulk of the ionized gas emitting in H α . As already mentioned, these two emission components show different kinematics, with the [OIII] 88 μm emitting gas being slower ($\sim 75 \text{ km s}^{-1}$) than the H α emitting gas ($\sim 600 \text{ km s}^{-1}$),

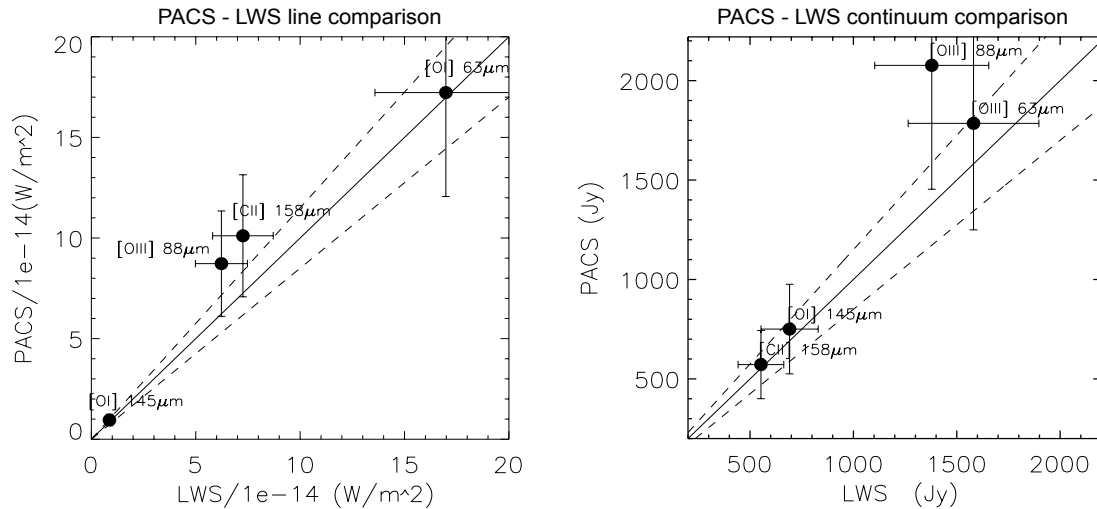


Fig. 8. Comparison between the LWS and PACS fluxes for lines (*left panel*) and continuum (*right panel*). The solid line indicates equal PACS and LWS fluxes, the dashed show a range of $\pm 15\%$. See text for details.

Shopbell & Bland-Hawthorn 1998). We have also seen that the [OIII] 88 μm emitting gas does not show any line splitting, contrary to what has been observed in the outflowing gas emitting in $\text{H}\alpha$. The $\text{H}\alpha$ line splitting in the outflow of M 82 has been interpreted as due to the confinement of the $\text{H}\alpha$ emitting gas in the walls of the outflow (Greve et al. 2004). These facts suggest a possible different spatial distribution of the ionized gas traced by the $\text{H}\alpha$ and the [OIII] 88 μm lines: while the first is confined in the outflow walls, the second is more concentrated along the minor axis of the galaxy.

This may also suggest that these gas components are ionized by two different physical processes. In fact, in the commonly accepted scenario, the bulk of the $\text{H}\alpha$ emitting gas is confined in the walls of the outflow, because it arises, at least in part, from shocked gas in the region of interaction between the X-ray emitting gas and the halo. This naturally explains the observed $\text{H}\alpha$ line splitting. Instead, the [OIII] 88 μm line may arise principally from ionization due to the starburst photons. Although we do not have enough data available to prove that this is the case, previous results seem to support this scenario. Shopbell & Bland-Hawthorn (1998) show that in the southern outflow, the optical [NII]/ $\text{H}\alpha$ ratio is lower along the minor axis than further away from the axis, probably reflecting a higher ionization. This is interpreted as radiation produced by the two star forming clusters in the disk escaping along the minor axis of the disk. Veilleux et al. (2009) reached a similar conclusion for both parts of the outflow studying the variation of the ratio between the near-infrared H_2 and the PAH emission.

We can summarize the main results obtained in this section as follows. Both neutral and ionized atomic gas are detected in the outflow and in the disk. In the outflow, the ionized gas emitting in the [OIII] 88 μm line is more collimated than the neutral gas and also than the ionized gas emitting in $\text{H}\alpha$, which is more confined in the walls of the biconical outflow. The ionized gas traced by the [OIII] 88 μm line and the neutral atomic gas show the same kinematics in the disk and in the outflow which differ from the kinematic of the $\text{H}\alpha$ emitting gas. These facts suggest a scenario where, while the $\text{H}\alpha$ filaments in the outflow arise, at least in part, from shocked gas in the regions of interaction between the outflowing hot plasma emitting in X-ray and the halo of the galaxy, the bulk of the [OIII] 88 μm line emission arises from gas photoionized by the starburst radiation along the

galaxy minor axis. The comparison between the optical and infrared emission suggests that the base of the northern outflow is more extinguished than the southern one, probably obscured by the disk itself.

4. Analysis

In this section, we will address the origin of the neutral material detected with PACS, with particular focus on its origin in the outflow. We have seen that this is certainly material contributing to the outflow and the question is whether this emission can be explained by classical photodissociation-regions (PDRs) emission and, if this is the case, how the physical conditions of the PDRs in the outflow and in the galaxy disk compare to each other. We will also compare the energetics and the kinematics of the neutral medium with that of the other gas phases detected in the outflow of M 82.

4.1. Photo-dominated regions diagnostics

The [CII] and [OI] lines are the main coolants of the atomic medium. They are collisionally excited by the atomic gas heated from electrons ejected from grains via photoelectric effects. Since C^+ has an ionization potential equal to 11.3 eV, it is mainly excited by far UV (FUV) photons ($h\nu < 13.6$ eV) escaping from HII regions (but it can also be excited in the HII regions themselves as we will discuss in Sect. 4.1.3). The regions where FUV photons dominate the ISM physics are called photodominated or photodissociation regions (PDRs, Hollenbach & Tielens 1999, and reference therein). Since the atomic gas cooling is mainly traced by the [CII] and [OI] line at 63 μm and the heating is due to the photoelectric effect on the grains, the ratio between the total emission from the FIR fine structure lines and the total infrared (TIR) emission from grains gives the total photoelectric yield. Comparing the observed yield with that predicted by the model one can derive fundamental physical parameters of the neutral ISM associated with the PDRs.

In this section, we will show the results obtained by applying the PDR model from Kaufman et al. (1999) to the PACS data of M 82. By applying the model to each pixel of our maps, we are able to produce, for the first time for an extragalactic object, high resolution, fully sampled maps of the FUV interstellar radiation

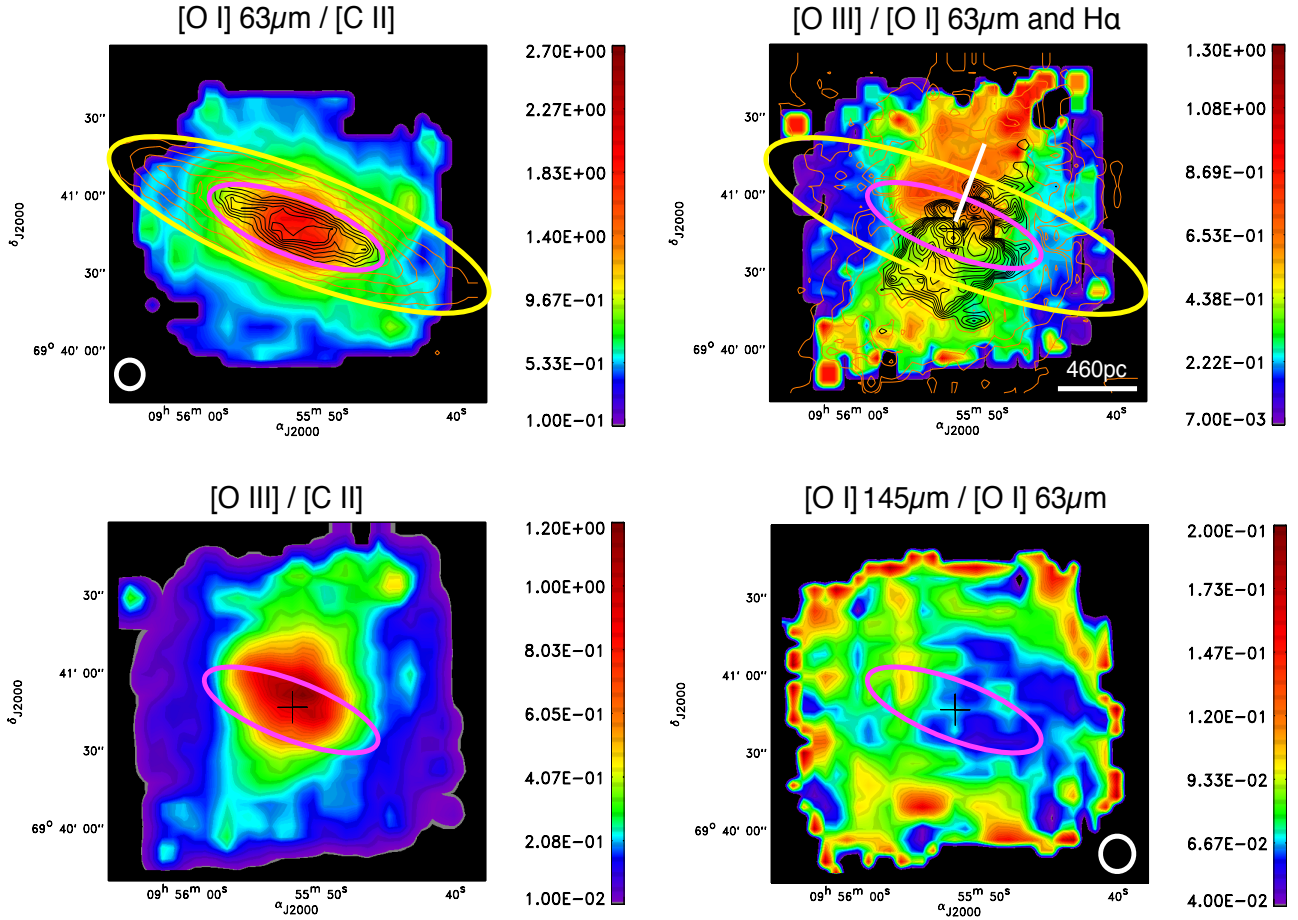


Fig. 9. [OI] 63 μm /[CII], [OIII] 88 μm /[OI] 63 μm , [OIII] 88 μm /[CII] and [OI] 145 μm /[OI] 63 μm ratio maps. The K_s -band contours are overplotted on the [OI] 63 μm /[CII] ratio map. They were used to define the outer ellipse tracing the stellar disk and the inner ellipse that delineates the starburst region. H α contours are overplotted on the [OIII] 88 μm /[OI] 63 μm ratio map. The white line along the minor axis of the northern outflow, indicates a linear size of 450 pc. (This figure is available in color in the electronic form.)

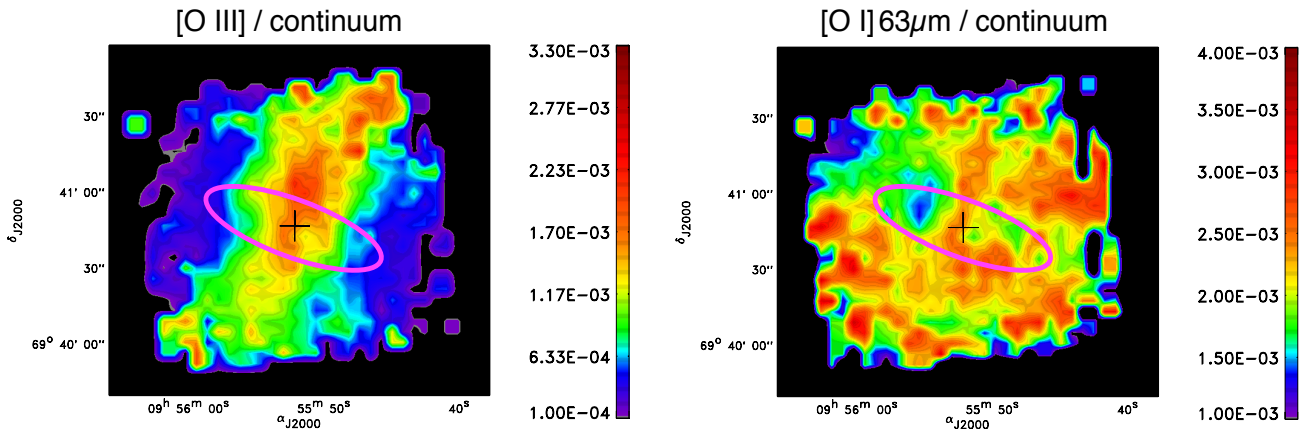


Fig. 10. [OIII] 88 μm /continuum (left) and [OI] 63 μm /continuum (right) ratio maps. The continuum is from the baseline level of the line fit. (This figure is available in color in the electronic form.)

field (ISRF) expressed in G_0 units², of the neutral gas density n_{H} , of the gas temperature at the surface of the modeled clouds T_{S} and of the cloud beam filling factors ϕ . Because of different step sizes in mapping among all wavelengths and final dimensions of the various continuum maps, we rebinned all maps to the grid

² G_0 is the FUV (6–13.6 eV) ISRF normalized to the solar neighborhood value expressed in Habing flux: 1.6×10^{-3} erg s⁻¹ cm⁻².

used for the longer wavelengths mapping (6''/pix), reduced all images to the same size, smoothed all maps to the coarser spatial resolution of the [CII] map, then aligned all to the [CII] emission peak. In the following analysis we will assume that the [CII] and [OI] lines arise from PDRs also in the outflow, and we will check a posteriori if this makes physically sense. However, in order to correctly and successfully apply the PDR diagnostics one has to make some corrections to the observed fluxes that we will

explain in detail in the following sections, before showing the results.

4.1.1. Total infrared emission map calculation

One fundamental input to the PDR modeling is the total IR emission (TIR from ~ 30 to $1000 \mu\text{m}$). Since our aim is to derive a solution for every pixel of the M 82 mapped area, we need to have also the TIR emission in each pixel. But the IR continuum data available from previous observations (IRAS, ISO, *Spitzer*) do not have the spatial resolution that matches that of PACS at these wavelengths. Fortunately, thanks to the brightness of M 82, we could use the continuum detected aside the targeted lines and in the corresponding parallel channel, as photometric points from which we could derive the FIR (from ~ 40 to $200 \mu\text{m}$) emission at each pixel. This gives a total of 8 points per pixel at 63, 72.8, 78.9, 145, 157, 176.8 and $189.6 \mu\text{m}$. We fit the continuum fluxes with a modified blackbody, in the optically thin emission approximation and with a fixed value of the grain emissivity, i.e. with $\beta = 1$ in each pixel. However, the agreement of the set of continuum data points obtained from the blue band lines and the corresponding red parallel points do not agree very well with those obtained from the continuum aside the red lines and the corresponding blue parallel data. In particular, the data derived from the parallel channels of the [CII] and [OI] line at $145 \mu\text{m}$ (i.e. 72.8 and $78.9 \mu\text{m}$) are often systematically higher than the data values at the other wavelengths. The reason for this is not well understood, but it might correspond to an higher continuum distortion at these wavelengths introduced from the bright line mode with respect to other wavelengths which increases the uncertainties.

Therefore we restrict the fitting to the 4 photometric points calculated on the blue lines and the corresponding parallel data. In this way we include in the gray body fitting the point at the highest possible wavelengths, allowing a better determination of the far infrared emission. An example of such a fit is shown in Fig. 11 for one pixel. From the black body fit, for each pixel we calculated the flux density at 60 and $100 \mu\text{m}$ which is necessary for the comparison with diagnostics used in the pre-*Herschel* era, and from these flux densities we derived the FIR (from 42.5 to $122.5 \mu\text{m}$) emission using the Helou (1988) formula:

$$FIR(W/m^2) = 1.26 \times 10^{-14} \times (2.58 \times I_{60 \mu\text{m}}(\text{Jy}) + I_{100 \mu\text{m}}(\text{Jy})). \quad (1)$$

The blackbody fitting also results in a dust temperature for each pixel that we used to build the map shown in Fig. 12 where also the $H\alpha$ contours and the smaller of the two ellipses shown in previous figures are shown. Taking into account the flux uncertainties we estimated an uncertainty on the dust temperature of ± 3 K. The dust temperature image shows very clearly the bright central region included in the ellipse and corresponding to the brightest $H\alpha$ emission. Here the dust temperature ranges from ~ 45 to ~ 55 K, typical for a starburst region. In the map is also visible an extension of the dust emission above the disk along the minor axis which coincides with the $H\alpha$ extension along this direction and with the outflow seen in the [OIII]/[OI] $63 \mu\text{m}$ ratio map. The dust in the southern outflow is slightly hotter than in the northern outflow.

From the FIR emission we calculate the TIR emission needed as input to the Kaufman et al. (1999) model by using Eq. (3) given in Dale et al. (2001) which calculates the conversion from FIR to TIR from the 60/100 μm ratio.

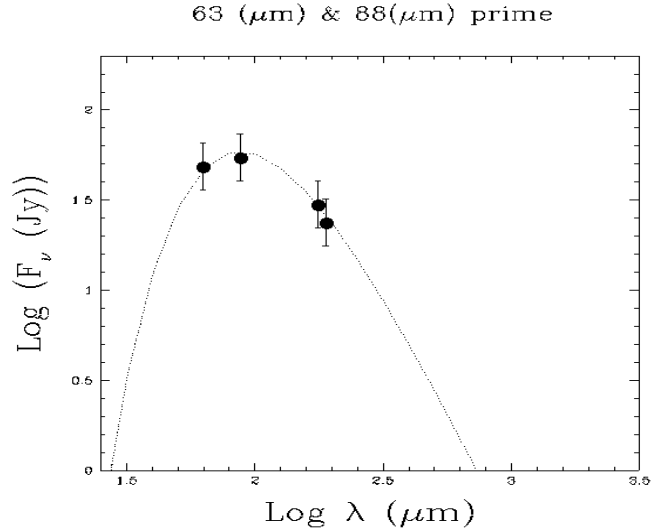


Fig. 11. Example of a modified blackbody fit on one pixel in the center of M 82. The points correspond to the continuum averaged detected with PACS on both sides of the [OI] line at $63 \mu\text{m}$ and [OIII] at $88 \mu\text{m}$ and on the corresponding parallel channel.

4.1.2. Geometrical effect correction factor

The PDR model we consider in this work assumes the emission is generated by a one-dimensional semi-infinite slab illuminated from one side. The model also considers [CII], FIR and [OI] at $145 \mu\text{m}$ optically thin, and [OI] at $63 \mu\text{m}$ optically thick, such that in a model where a cloud is illuminated from one side, only one side of the cloud emits in the [OI] line at $63 \mu\text{m}$ while [CII], FIR and [OI] at $145 \mu\text{m}$ emits from both the front and the back of the cloud. At the PACS resolution each beam includes many clouds, and the orientation of the illuminated side will be randomly distributed. This is equivalent to consider that the beam includes one cloud illuminated from all sides. The model would then predict half of the [OI] at $63 \mu\text{m}$. This is why we multiply the observed [OI] at $63 \mu\text{m}$ by 2 before applying the PDR models. Since the [OI] at $145 \mu\text{m}$ is considered to be thin in the model, we do not have to apply any correction to it.

4.1.3. Contribution to the [CII] emission from the ionized gas

[CII] can also arise from the ionized medium. Since the PDR model considers [CII] arising only from the neutral medium, before applying the model to the observations we have to subtract this contribution from the observed [CII] emission. The percentage of the [CII] emission arising from ionized gas with respect to the total observed emission, is minimum ($\sim 10\%$) in dense HII regions, since here most of the carbon is double ionized, but it increases significantly in the diffuse ionized medium, the precise amount depending on the physical parameters of the medium (Nagao et al. 2011). In external galaxies the beam typically encompasses regions with very different physical conditions, therefore one has to guess the average properties of the observed medium in each spatially resolved region, in order to estimate the [CII] contribution from ionized gas. This will obviously introduce some uncertainty in the derived parameters.

The most straightforward way to determine the fraction of [CII] arising from the ionized medium is to use the scaling relation between the ($^3P_1 \rightarrow ^3P_0$) [NII] line at $205.178 \mu\text{m}$ and the [CII] line (Abel 2006). Since these have similar critical electron densities (80 and 50 cm^{-3} respectively), their ratio

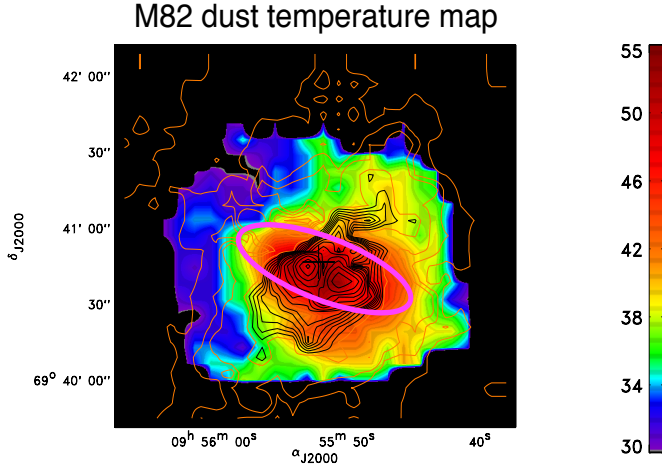


Fig. 12. Dust temperature map. Units are °K. $H\alpha$ contours are overplotted. Note that these contours are at a resolution poorer than what is shown in Fig. 9 to match the pixel size of the dust temperature map. (This figure is available in color in the electronic form.)

is almost independent on the electron density. Unfortunately, we cannot use this method because we did not observe M 82 in the [NII] 205 μm line with PACS. A less direct, and more uncertain, way to calculate the contribution from ionized gas to the observed [CII] line flux, is to use the [NII] 122 μm line. Since [NII] 122 μm has a higher critical electron density ($3.1 \times 10^2 \text{ cm}^{-3}$) than that of the [CII] line, the ratio of these lines depends strongly on the density.

We have observed M 82 in the [NII] 122 μm line with three PACS spectrometer pointings centered on the disk, and on the north and south outflow as shown in Fig. 13. We have divided the galaxy in four regions: the starburst, the north and the south outflow and the more diffuse disk and we have calculated the mean [NII] emission for each of them using the average of the spectra belonging to each of the defined regions. The resulting average [NII] intensities in the starburst, disk, and in the northern and southern parts of the outflow are 87.4, 1.0, 5.3 and $3.4 \times 10^{-17} \text{ W m}^{-2}$. We assume that in the disk and in the starburst region of M 82 the [CII] fraction arising from ionized gas scales with the observed [NII] following the relation valid for the dense HII regions and for a Milky Way C/N abundance ratio equal to 3.8, Rubin et al. (1988, 1993):

$$[\text{CII}]_{\text{ionized}}^{\text{Disk}} = [\text{CII}]_{\text{dense HII}}^{\text{Disk}} = 1.1 \times [\text{NII}]^{\text{Disk}}. \quad (2)$$

In a recent work, Croxall et al. (2012), show how the [CII]/[NII] 122 ratio varies with electron density (their Fig. 11). We do not have a direct electron density measure in the outflow but we know from previous works that the average electron density of the ionized gas traced by the $H\alpha$ is $\sim 15 \text{ cm}^{-3}$ (Shopbell & Bland-Hawthorn 1998) and the estimated averaged electron density in the outflow is $\leq 300 \text{ cm}^{-3}$ (Yoshida et al. 2011). Since we do not know a priori from which of these media the [CII] arises, we have calculated the amount of [CII] arising from ionized gas for these two cases by using the ratio published by Croxall et al. (2012). From this work we derive a [CII]/[NII] 122 ratio equal to 3.7 and 0.7 for $n_e = 15$ and $n_e = 300 \text{ cm}^{-3}$. Note that these two density values correspond more or less the minimum and the maximum correction possible, in order not to have negative [CII] results. In each case, the resulting [CII] fluxes were then subtracted from the observed [CII] map, in the region defined as outflow. The resulting percentages of the [CII] emission arising from the ionized gas are

Table 1. Main PDR physical parameters obtained by modeling the [CII], [OI] 145 and FIR emission with and without correcting the observed [CII] line flux from the contribution from various ionized gas (see Sect. 4.1.3 for details).

[CII] correction applied	G_0	n_H cm^{-3}	T_{gas} K	ϕ %	τ_{CII}
Starburst					
No correction	1400	760	460	6.5	0.06
Dense HII region	2500	900	470	5.5	0.03
Disk					
No correction	400	200	380	1.6	0.1
Dense HII region	450	220	390	2.4	0.05
North outflow					
No correction	340	380	300	2.3	0.03
$n_e = 15 \text{ cm}^{-3}$	960	600	390	1.5	0.02
$n_e = 300 \text{ cm}^{-3}$	430	450	320	1.7	0.03
South outflow					
No correction	350	210	350	1.0	0.06
$n_e = 15 \text{ cm}^{-3}$	1200	420	440	1.2	0.03
$n_e = 300 \text{ cm}^{-3}$	390	210	420	1.6	0.04

Notes. The listed values are calculated by averaging the maps shown in figures from 14 to 17, over the four macro regions we have divided the galaxy in: starburst, disk, north and south outflow (see Fig. 18 for a schematic visualization of these regions). Last column lists the averaged value for the [CII] opacity maps obtained as explained in Sect. 4.3.

~ 10 , 30% in the disk and in the starburst, and ~ 11 (47)% and ~ 11 (40)% in the north and south cones of the outflow based on $n_e = 300$ (15) cm^{-3} respectively.

We stress, however, that these estimates of the contribution to the observed [CII] flux from pure ionized medium are very uncertain especially when applied to regions with an unknown and complex mix of different ISM phases. Moreover, because of the lack of a fully sampled map in the [NII] 122 μm line map, we were forced to use an average value of the [NII] 122 emission for each of the four macro-regions we have defined in the galaxy. It is for this reason that we decided to run the model also with and without the corrections to the observed [CII] emission line we have explained above, to check whether the main results we derive from the modeling are independent of the correction applied.

Moreover, in principle we could have used as input for the PDR modeling the two [OI] lines, [CII] and TIR. We have tried this but the uncertainties in each of the line is such that the result is much noisier than using 3 input values with only one [OI] line at the time. Therefore, we run the model using always only three input values, i.e. the [CII], the FIR and one of the [OI] lines at the time, and with and without the ionized contribution correction to the [CII] emission line (i.e. 6 input sets in total).

4.2. Results from the PDR modeling

By applying the PDR model for each input data set, we obtained G_0 and n_H for each pixel where all three input values are detected. From G_0 and n_H we then derived the corresponding gas temperature at the surface of the modeled cloud (T_S) and the area beam filling factor (ϕ), i.e. the percentage of the beam covered by the emitting clouds, obtained by dividing the [CII] emission corresponding to the G_0 and n_H solutions and the input [CII] value. Since this can be done for each pixel we were able to obtain 6 such maps for each input dataset defined as explained in the previous section. We stress, however, that given the flux uncertainties and the fact that a model is an oversimplification of much

more complex real physical conditions, we estimate the uncertainties of the derived PDR model parameters to be a factor ~ 2 . Also we do not really trust the pixel-to-pixel variation in the PDR solution maps, simply because the model uses a discrete grid, and given the flux uncertainties it is possible that a resulting solution is higher or lower than the solution it would have been assigned with smaller uncertainties. Sometimes this is visible in a hot/cold pixel in a middle of a well defined morphological structure, and we corrected for these interpolating with the neighborhood pixels.

Figures 14 to 17 show the 6 maps obtained using the six sets of inputs, for each of the above mentioned physical parameters. In detail: the top panels show the solutions obtained using as input to the PDR modeling [OI] 63, [CII] and FIR. Two of these maps were obtained by correcting the observed [CII] emission from the contribution arising from ionized gas assuming electron densities equal to 300 and 15 cm^{-3} in the outflow and applying Eq. (2) in the disk and starburst regions. The third solution was obtained without correcting the observed [CII]. The bottom panels of Figs. 14 to 17 show the three sets of solutions obtained in a similar way but using as input to the model the [OI] line at $145 \mu\text{m}$ instead of the [OI] line at $63 \mu\text{m}$.

All maps are very similar in morphology except for the gas density maps (Fig. 15). In particular, this figure shows that the gas density is enhanced in the starburst region for all the solutions obtained using the [OI] line at $63 \mu\text{m}$, and in the northern part of the starburst when the [OI] line at $145 \mu\text{m}$ is used.

We find that this difference is most likely due to misalignment between the [OI] $63 \mu\text{m}$ and [CII] images. We explain this in details in the Appendix A. Once this misalignment has been corrected, the morphologies of the images obtained by the PDR modeling for all parameters, included the density n_{H} , agree (see Fig. A.1), and the values agree within a factor of \sim two for all maps, except the density map for which the biggest difference is close to a factor of ~ 3 .

Because of the problems and uncertainties discussed above, and the fact that the [OI] $63 \mu\text{m}$ optical depth can significantly vary in the galaxy, we will use for the following analysis only the results obtained by using as input the [OI] $145 \mu\text{m}$ line. This reduces the uncertainties of our analysis to those related to the [CII] correction for ionized gas, since the [OI] $145 \mu\text{m}$ line is optically thin. Moreover, the pointing variation and the the processing affects the [CII] and [OI] $145 \mu\text{m}$ maps in a similar way, since they have been observed in the same AOR. The main uncertainty left, i.e. that due to the [CII] correction for the ionized gas contribution, can be assessed by examining the results obtained from the corrected and the not corrected [CII] values.

Therefore, we now concentrate on the results shown in the bottom panels of Figs. 14 to 17. The first thing to notice is that, for each of the derived maps, there is no significant difference in the morphology among the solutions obtained with no [CII] correction, and those with the two different corrections we have applied to the observed [CII] flux. We have calculated the average values of G_0 , n_{H} , T_{gas} and ϕ in the four regions we have considered for the different correction to the observed [CII], for each case, and listed them in Table 1. The ranges of values of the PDR solution parameters are all comparable within the uncertainties (a factor of 2 \sim 3). We are thus confident that the correction we have applied to the observed [CII] does not really play a major role.

As already mentioned, the gas density maps, show a density enhancement in the upper part of the starburst region, corresponding also to the brightest emission in the [OIII]/[CII] ratio map shown in Fig. 9.

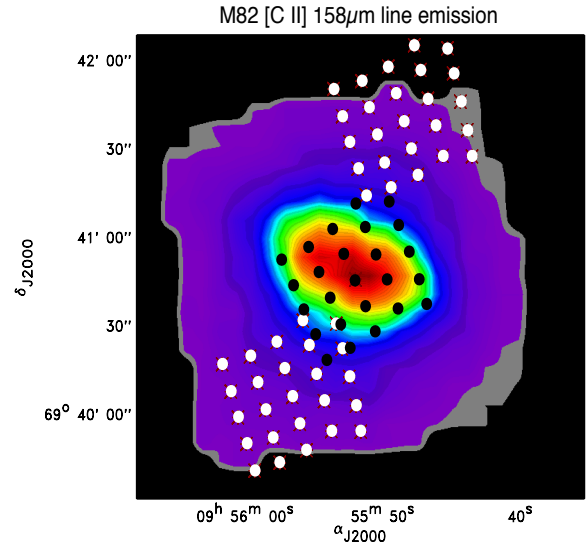


Fig. 13. The PACS spectrometer footprints of the 3 pointings executed in [NII] $122 \mu\text{m}$ are overplotted on the [CII] intensity map of M 82 (the same as shown in Fig. 2). Note that the size of the circles does not represent the size of a spaxel on the sky. (This figure is available in color in the electronic form.)

The gas temperature is everywhere greater than $\sim 300 \text{ K}$ as we had already deduced from the constancy of the two [OI] lines ratio map. The brightest emission outlines the disk of the galaxy and no structures corresponding to the outflow are visible.

The PDR area filling factor maps are very similar in all cases and show that there is an enhancement in the galaxy disk with a slight asymmetry toward its northwestern part. The area filling factors in the outflow are significantly smaller than in the disk and very similar to the diffuse more spherically distributed emission visible in all line intensity maps.

One interesting result common to all solutions is that we mapped an area sufficiently large to detect relatively diffuse emission from the galaxy disk, with $G_0 \sim 100$ and $n_{\text{H}} \sim 50 \text{ cm}^{-3}$. Previous space missions have not had the sensitivity or spatial resolution to detect FIR fine structure lines from the low density cold atomic medium of galaxies. As demonstrated by our results, *Herschel* will greatly advance the study of the multi-phase ISM in external galaxies in the FIR.

Figure 18 shows the logarithmic plot of G_0 versus n_{H} for all solutions obtained with the input sets which included the [OI] line at $145 \mu\text{m}$. Similar plots derived using the results obtained with the re-aligned [OI] $63 \mu\text{m}$ map, are consistent with those shown in Fig. 18. The macro regions defined for the different corrections to the [CII] total flux are sketched in the top right panel. The same color code is used in the three plots shown in the figure. The upper panel shows the results obtained using as input to the model the observed [CII] emission without any correction; the bottom left (right) panel shows the results obtained assuming that the electron density of the ionized gas producing [CII] to be subtracted to the observed flux is equal to 300 (15 cm^{-3}). The similarity between all relationships is evident, reinforcing our assertion that the correction to [CII] does not significantly impact our results. This figure shows that n_{H} and G_0 are correlated and that the correlation agrees with what was previously found by Malhotra et al. (2001) by modeling a sample of local star-forming galaxies observed with the infrared space observatory (ISO-LWS) and that are shown as yellow asterisks in Fig. 18. Also shown in this figure is the value obtained from

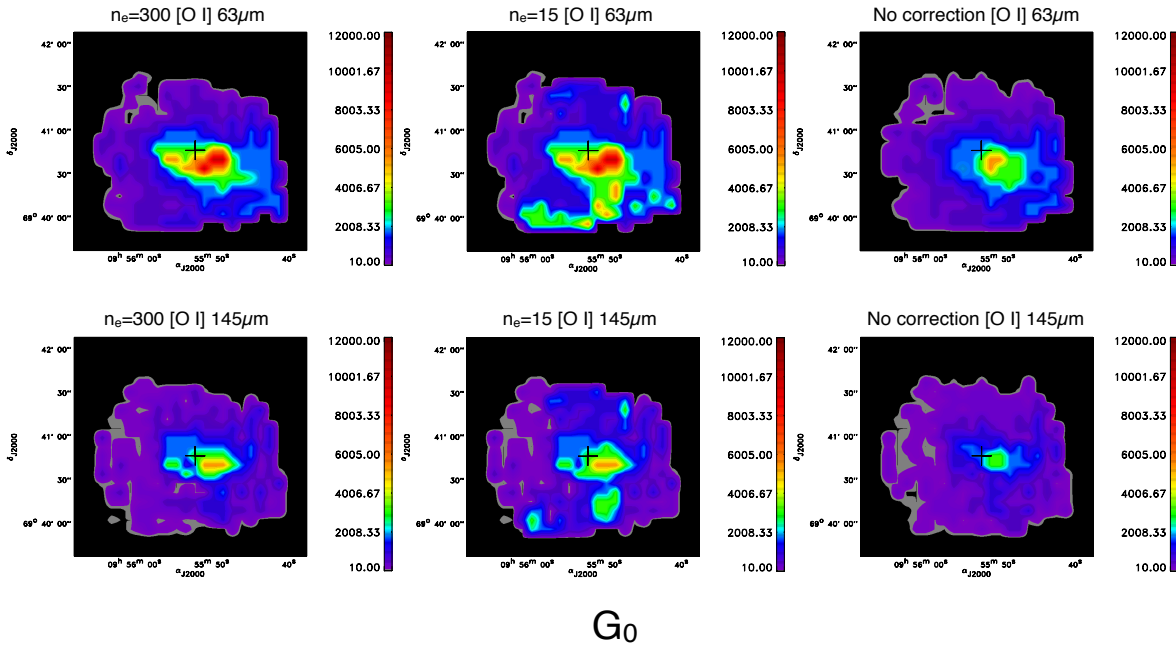


Fig. 14. The PDR solution maps obtained for the far UV interstellar radiation field in units of G_0 . Left to right are the results obtained correcting the [CII] flux from the ionized contribution obtained by considering the densities of the ionized gas equal to 300 (*left*) and 15 cm^{-3} (*middle*) and with no correction (*right*). The *top* row shows the results obtained using as input [OI] 63, [CII] and FIR; the *bottom* row shows the results obtained using as input [OI] 145, [CII] and FIR (see Sect. 4.3.1 for details). (This figure is available in color in the electronic form.)

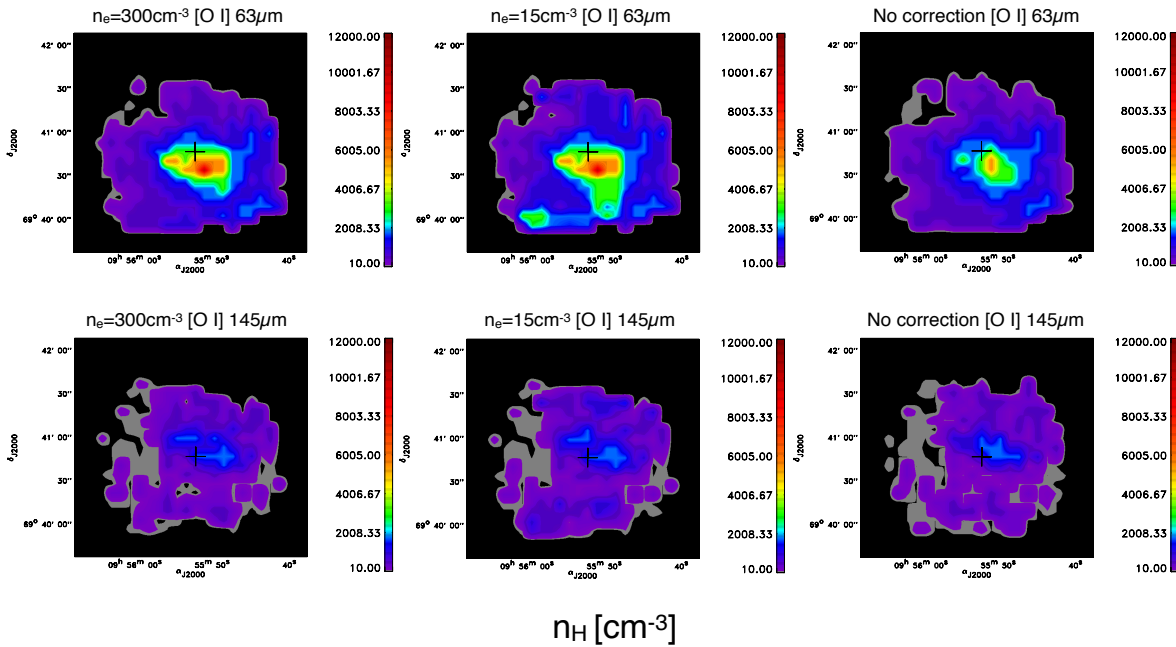


Fig. 15. The PDR solution maps obtained for the gas density n_{H} . (This figure is available in color in the electronic form.)

Colbert et al. (1999) from ISO–LWS observations of M 82. We find that the solutions for M 82’s starburst region corresponds well to the PDR solution determined by Malhotra et al. and

Colbert et al. from the ISO data. The ISO-LWS observations are single pointings centered on the galaxy centers (i.e. do not encompass the entirety of the disk) and therefore are biased

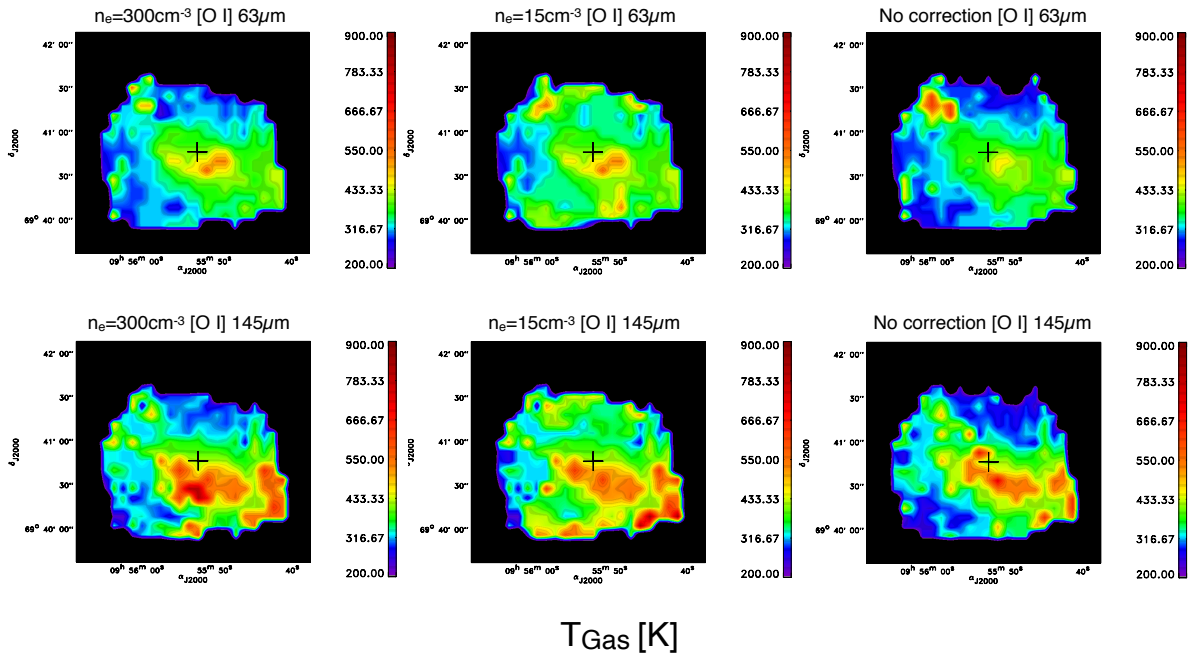


Fig. 16. The PDR solution maps obtained for the temperature of the gas T_{gas} . (This figure is available in color in the electronic form.)

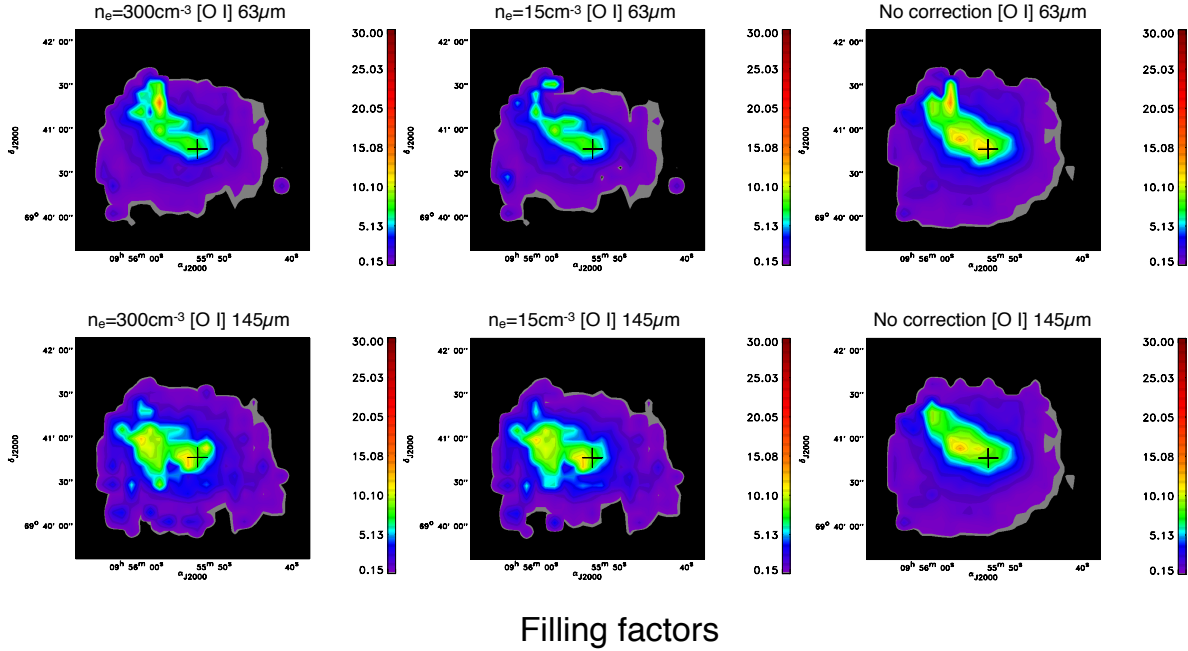


Fig. 17. The PDR solution maps obtained for the area beam filling factor ϕ , i.e. the percentage of the beam covered by the emitting clouds. (This figure is available in color in the electronic form.)

towards the warm and dense central regions. This explains why these measurements occupy the high $G_0 - n_{\text{H}}$ part of the diagram. The results of this work extend the correlation by almost 2 orders

of magnitude to much lower $G_0 - n_{\text{H}}$. All four components of M 82 that we considered, follow the same correlation in $G_0 - n_{\text{H}}$ as normal galaxies suggesting a common origin of the neutral

gas emission for all regions, including the outflow. This means that the neutral gas as traced by its main coolants is consistent with arising by classical PDRs also in the outflow.

4.3. Column density and [CII] optical depth of the atomic neutral medium associated with the PDRs

The averaged cloud column density of the hydrogen nuclei associated with the [CII] emission, $N_{\text{[CII]}}(\text{H})$, can be calculated using the following equation (Crawford et al. 1985):

$$N_{\text{[CII]}}(\text{H}) = \frac{4.25 \times 10^{20}}{\chi(C)} \left[\frac{1 + 2 \times e^{(-92/T)} + (n_{\text{crit}}/n_{\text{H}})}{2 e^{(-92/T)}} \right] \left[\frac{I_{\text{[CII]}}^{\text{PDR}}}{\phi} \right], \quad (3)$$

where $N_{\text{[CII]}}(\text{H})$ is in cm^{-2} , $I_{\text{[CII]}}^{\text{PDR}}$ in $\text{erg s}^{-1} \text{cm}^{-2} \text{sr}^{-1}$, ϕ is the area filling factor, i.e. the fraction of the beam filled with clouds emitting [CII], $\chi(C)$ is the $[\text{C}^+]/[\text{H}]$ gas-phase abundance ratio that is equal to 3×10^{-4} (Crawford et al. 1985), n_{crit} is the critical density for collision of C^+ with H atoms equal to $4 \times 10^3 \text{cm}^{-3}$, T is the gas temperature in K and n_{H} is the gas density. Using the observed (and corrected) [CII] emission, the temperature, the gas density and filling factor values resulting from the PDR modeling we are able for the first time to derive the averaged cloud column density map of the HI gas associated with the PDRs emitting the observed [CII] in M82.

The resulting column density ranges from $\sim 1 \times 10^{21} \text{cm}^{-2}$ up to $\sim 1 \times 10^{22} \text{cm}^{-2}$ for all input data sets except for the ones obtained using the [OI] line at $145 \mu\text{m}$ and [CII] not corrected for the ionized gas contribution, for which the column density reaches few 10^{22}cm^{-2} . We also derived the [CII] optical depth map by applying the following formula (Crawford et al. 1985):

$$\tau_{\text{[CII]}} = \frac{\lambda^3 A_{\text{ul}}}{8\pi\Delta\nu} \left[\left(1 + \frac{n_{\text{crit}}}{n_{\text{H}}} \right) e^{92/T} - 1 \right] \times \left(\frac{2 e^{(-92/T)}}{1 + 2 e^{(-92/T)} + (n_{\text{crit}}/n_{\text{H}})} \right) N_{\text{[CII]}}(\text{H}). \quad (4)$$

The results obtained are shown in Fig. 19. The morphology of both the average cloud column density (not shown here) and the [CII] opacity maps, are obviously similar. All maps have [CII] optical depths much less than 1. The last column of Table 1 lists the average $\tau_{\text{[CII]}}$ values of the starburst, the disk, the north and south part of the outflow. The map obtained with no correction to the observed [CII] line flux shows an opacity higher (up to ~ 0.1) than those obtained correcting the [CII] observed flux from ionized gas contribution, as expected, while the morphology is very similar in all three cases. Figure 19 shows that the opacity is higher along the disk of the galaxy with a decrease toward the starburst region, where the brightest $\text{H}\alpha$ emission is also located. This opacity decrease could be the result of material cleared out from the winds powering the outflow. The opacity drop is even more pronounced in the outflow regions, especially in the northern one.

Some estimates of the column density associated with the [CII] line emitting gas already exist for M82. In particular we compare our results with those obtained from Crawford et al. (1985). These authors derived $\tau_{\text{[CII]}} \lesssim 0.2$ and column density $N_{\text{CII}} \geq 9 \times 10^{17} \text{cm}^{-2}$ by using Eqs. (3) and (4) in the limit of high density ($n \gg n_{\text{crit}}$) and high temperature ($T \gg 92 \text{K}$). We have calculated a corresponding column density and optical depth averaging the values obtained from our maps, in a region

of M82 which corresponds, as close as possible, to the position and beam size used in the Crawford observations. We find an average $[\text{C}^+]$ column density a few 10^{18}cm^{-2} and an opacity ~ 0.03 , in good agreement with the limits given by Crawford et al. (1985) on these parameters.

4.4. Outflow energetics

We can estimate the minimum mass of the hydrogenic nuclei associated with the [CII] emitting gas using Eq. (1) of Hailey-Dunsheath et al. (2010),

$$\frac{M_{\text{[CII]}}(\text{H})}{M_{\odot}} = 0.77 \times \left(\frac{0.7L_{\text{[CII]}}}{L_{\odot}} \right) \times \left(\frac{1 + 2e^{(-92/T)} + n_{\text{crit}}/n}{2e^{(-92/T)}} \right), \quad (5)$$

in what follows, we calculate the mass, the kinetic energy and the mass outflow rate associated with the neutral atomic gas emission obtained in this work (Table 2) and we compare them to the corresponding values of the cold molecular gas traced by the CO emission, the warm molecular gas traced by the H_2 emission and the ionized gas emitting in $\text{H}\alpha$ (Table 3).

Using Eq. (5) we calculate the neutral atomic gas masses associated with the outflow for each input data set involving the [OI] line at $145 \mu\text{m}$ only (listed in Col. 1 of Table 2). The overall uncertainties for these quantities are comparable with those quoted for the PDR parameters.

The total atomic mass in form of PDRs in the outflow is $2\text{--}8 \times 10^7 M_{\odot}$ depending on the input data, a factor $\sim 4\text{--}15$ times lower than the cold molecular mass entrained in the outflow as measured by Walter et al. (2002, $M \sim 3.3 \times 10^8 M_{\odot}$) and 3 orders of magnitude higher than the warm molecular gas (Veilleux et al. 2009). Our values should be regarded as lower limits because the area on which we have calculated the outflow masses, is not defined by the intensity of the emission but by the extent of the mapped area. In other words, there may be still material further out that we have just not mapped. Moreover, this is not the total atomic mass carried in the outflow but only that associated with the [CII] emitting gas. Therefore the atomic and molecular gas in the outflow could be considered as almost comparable. For comparison, the mass of the warm filaments detected at optical wavelengths is $5.8 \times 10^6 M_{\odot}$ (Shopbell & Bland-Hawthorn 1998).

The kinetic energy associated with the neutral gas is $E_{\text{kin}} = M_{\text{[CII]}}(\text{H}) \times v^2$ where v^2 is the deprojected mean velocity of the outflow calculated as explained in Sect. 3.3. We obtained values in the range of $\sim 1\text{--}5 \times 10^{54} \text{erg}$ (Table 2, Col. 2) for the two cones of the outflow. From Table 3 we see that these values are 1 order of magnitude lower than what is found from the outflowing molecular gas (Walter et al. 2002) and $\text{H}\alpha$ gas (Shopbell & Bland-Hawthorn 1998) equal to $\sim 3 \times 10^{55} \text{erg}$. These values are also ~ 2 orders of magnitude higher than the kinetic energy of the warm H_2 molecular gas calculated by assuming that the velocity of the warm molecular gas is equal to that of the CO molecular gas (Veilleux et al. 2009). Therefore, although not energetically dominant, the atomic gas in the outflow still represents a significant contribution to its overall energetic.

We define the dynamical time of the outflow as the time necessary for its material to travel at a mean velocity equal to v_{deproj} up to a distance of 450pc away from the disk along the minor axis. We use this length because this is the extent of the mapped area above and below the galaxy's disk. We can apply this simple calculation to both the neutral and the ionized gas, the latter being traced by the [OIII] line emission. The dynamical time for both cones of the outflow is $\sim 5 \times 10^6 \text{yr}$ for the

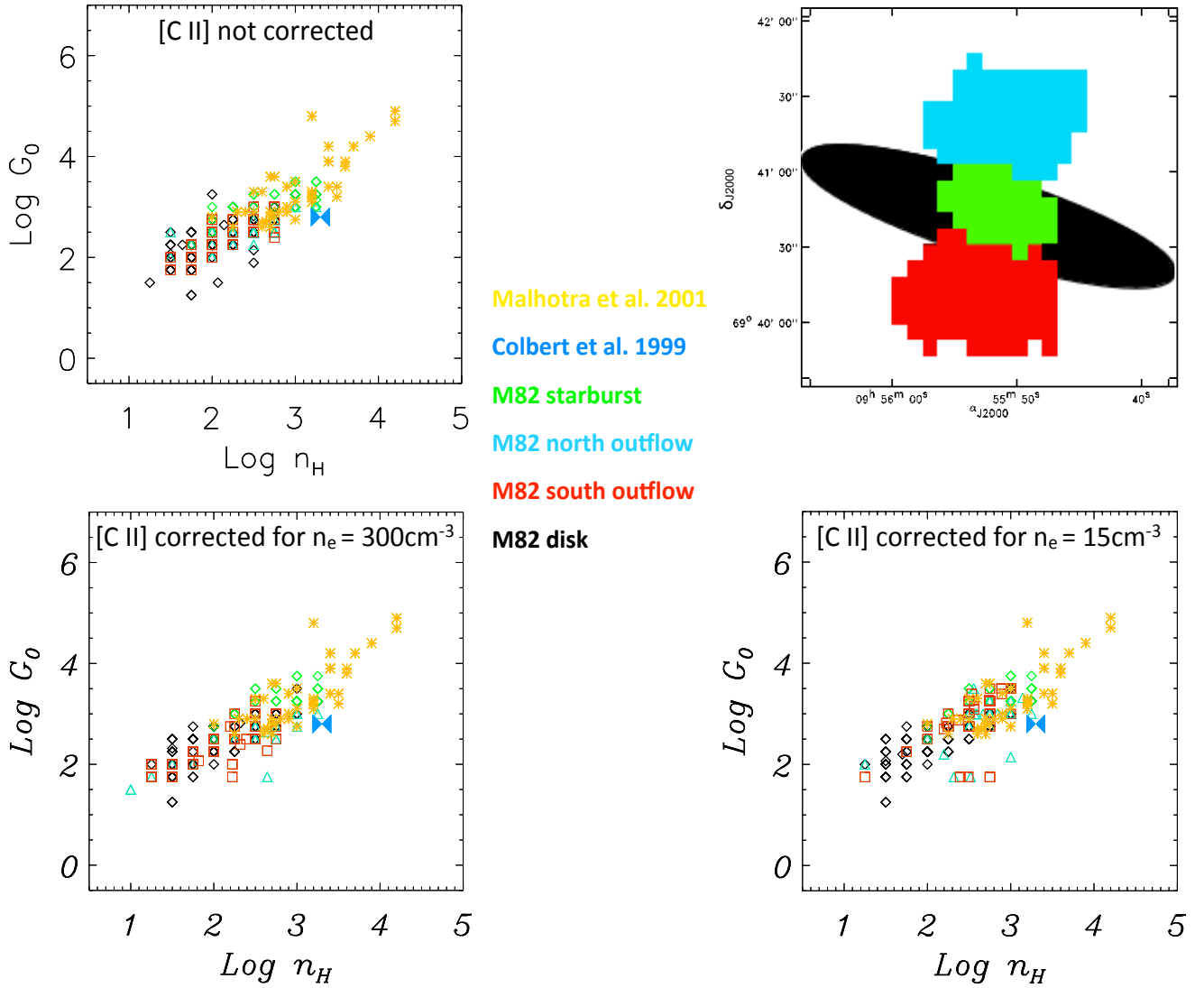


Fig. 18. PDR solutions for M82 obtained by using [CII], [OI] at $145\ \mu\text{m}$ and TIR as input parameters to the model. On the *right of the top panel* a schematic view of the masks used to define the starburst (green), the disk (black), and the north (cyan) and south (red) outflow is shown. The same color code has been used for the plotting. Also overplotted for comparison, the solutions obtained for a local sample of normal star forming galaxies from Malhotra et al. (2001) (yellow stars) and with the ISO-LWS single pointing flux of M 82 (Colbert et al. 1999). *Top*: PDR solutions obtained by using as input the [CII] emission not corrected for the ionized gas contribution. *Bottom left*: the results obtained by using the [CII] corrected for the ionized gas contribution assuming a electron density equal to $300\ \text{cm}^{-3}$. *Bottom right*: the results obtained by using the [CII] corrected for the ionized gas contribution assuming a electron density equal to $15\ \text{cm}^{-3}$. See Sect. 4.1.3 for details. (This figure is available in color in the electronic form.)

neutral and the ionized gas, basically because they all have comparable deprojected mean velocities in the outflow. This time is also comparable to that estimated for the warm molecular H_2 by Veilleux et al. (2009) for the same distance we have assumed in our calculation.

Finally we can calculate the mass outflow rate of the neutral gas in the outflow dividing the masses by the dynamical times. For each input data set, the mass outflow rates (Col. 3 of Table 2) are similar in the northern and southern cones of the outflow. The range of the total neutral gas mass rate is $10\text{--}25\ M_\odot/\text{yr}$. However, if we add the mass outflow rate of the molecular component in the outflow ($33\ M_\odot/\text{yr}$, Walter et al. 2002) the total PDR outflowing mass rate in the outflow is comparable to the total Star Formation Rate (SFR) of M 82 ($\sim 25\ M_\odot/\text{yr}$) estimated by Förster-Schreiber et al. (2003) giving a mass load (defined as $\dot{M}_{\text{Outflow}}/\text{SFR}$) ~ 2 similar to that measured in another starburst galaxy NGC 253 (Sturm et al. 2011).

4.4.1. Comparison amongst the various phases of outflowing material

We can summarize the ISM phases participating to the M 82's outflow as follows: the hot ($10^7\ \text{K}$) gas emitting in X-rays; the ionized cooler gas ($10^4\ \text{K}$) emitting in $\text{H}\alpha$; the cold and warm molecular gas (Walter et al. 2002; Veilleux et al. 2009), the cold ($\sim 300\text{--}400\ \text{K}$) neutral gas (this work) and the dust (Alton et al. 1999; Leeuw & Robson 2009; Kaneda et al. 2010; Roussel et al. 2010). These components are not all dynamically coupled to each other. The cold molecular gas traced by the CO emission and the neutral gas traced by the FIR fine structure line emission studied in this work have similar averaged velocities and opening angles which suggests they are coupled. These components are decoupled from the ionized gas emitting in $\text{H}\alpha$ which has much higher velocity (Greve 2004). If we assume that also the PAHs emission observed by Engelbracht et al. (2006) and

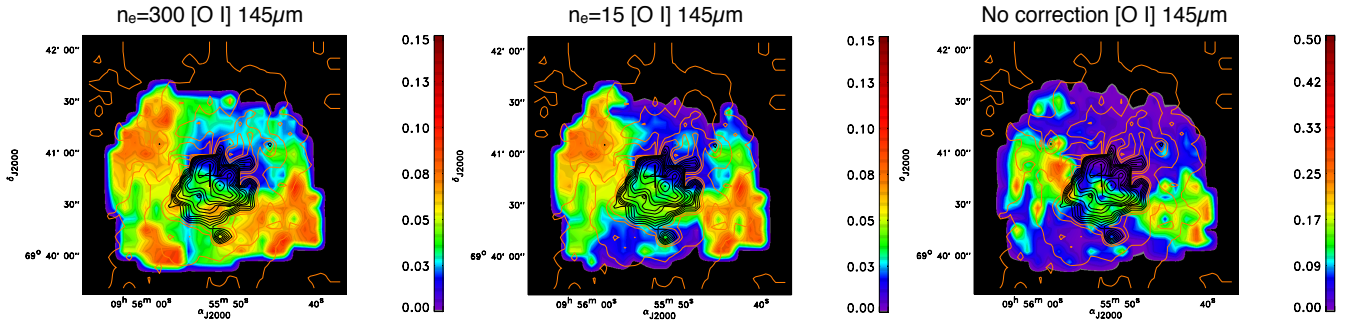


Fig. 19. The [CII] opacity maps obtained by using Eq. (4). Only the result of the modeling obtained using as input data set [CII] (with and without corrections), FIR and the [OI] line at $145\ \mu\text{m}$ are shown. (This figure is available in color in the electronic form.)

Table 2. Atomic gas characteristics in M 82 outflow.

Input set	$M_{[\text{CII}](\text{HI})}$ $10^7 M_{\odot}$	E_{kin} 10^{54} erg	\dot{M} M_{\odot}/yr
[OI] $145\ \mu\text{m}$, [CII] corrected $n_e = 15\ \text{cm}^{-3}$			
North	2.1	1.5	4.0
South	2.9	1.7	5.1
[OI] $145\ \mu\text{m}$, [CII] corrected $n_e = 300\ \text{cm}^{-3}$			
North	4.3	3.2	8.4
South	8.4	5.0	14.8
[OI] $145\ \mu\text{m}$, [CII] NOT corrected			
North	4.1	3.1	8.1
South	6.1	3.6	10.7

Table 3. Masses, kinetic energies and mass outflow rates in the outflow of M 82 for the cold, warm and ionized gas traced by the $\text{H}\alpha$ emission, obtained in other works.

Gas phases	$M_{[\text{CII}](\text{HI})}$ M_{\odot}	E_{kin} erg	\dot{M} M_{\odot}/yr	Reference
Cold molecular gas	3.3×10^8	3.3×10^{55}	33	Walter et al. (2002)
Warm molecular gas	1.2×10^4	10^{51}	0.001	Veilleux et al. (2009)
Ionized gas traced by $\text{H}\alpha$	5.8×10^6	2.0×10^{55}	3.6	Shopbell & Bland-Hawthorn (1998)
Neutral atomic gas	$2\text{--}8 \times 10^7$	$1\text{--}5 \times 10^{54}$	10–25	This work

Notes. These values should be compared with the values obtained for the neutral atomic emitting gas calculated in this work and listed in Table 1.

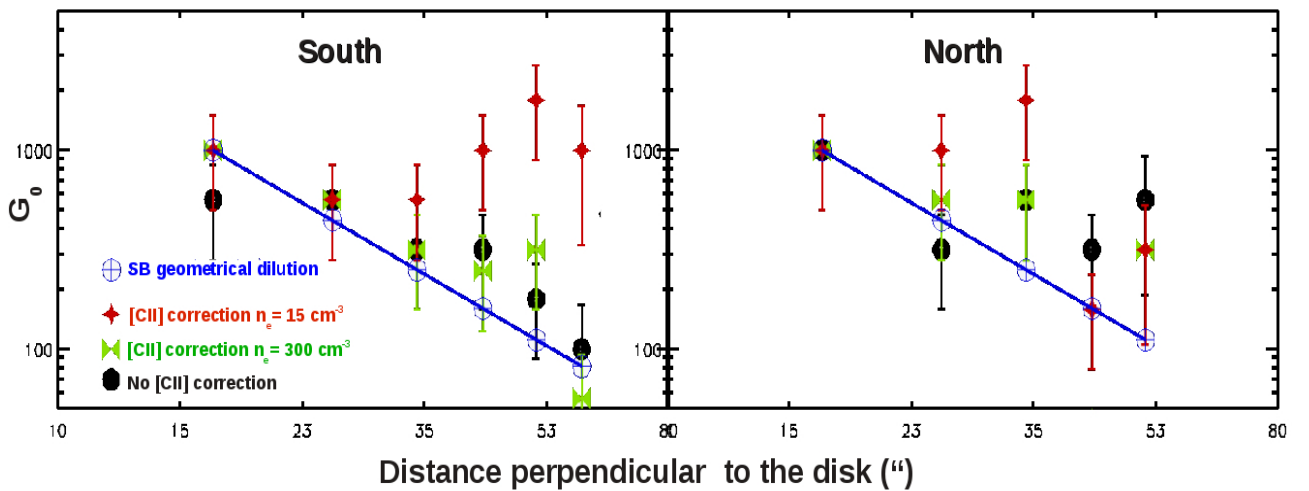


Fig. 20. The observed FUV ISRF in Habig units along the minor axis of M 82 are plotted as a function of the distance from the galaxy center in $''$, for the south (*left*) and north (*right*) outflow separately. The blue symbols connected by the blue line, are the values calculated in the pure geometrical dilution hypothesis. The starburst region, which occupies the central 250 pc ($\sim 15''$) is not included. (This figure is available in color in the electronic form.)

the warm molecular gas observed by Veilleux et al. (2009), for which we do not have kinematic information, are also coupled with the [CII] emitting gas in the outflow, we have gathered all fundamental components of the classical PDRs.

Probably, the cold gas material is entrained from the disk into the outflow by the fast hot wind, in the form of clouds. Once in the outflow, the UV photons in the wind itself and/or directly from the starburst region, excite the external shells to these clouds which emit in the observed FIR fine structure lines, the aromatic bands from PAHs and warm molecular gas traced by H_2 in the near infrared. Micelotta et al. (2005) have shown that PAHs can survive the destruction by collisions with thermal electrons in the hot winds only if they are in form of cold cloudlets. This supports the idea of having the molecular and cold neutral medium in the outflow organized in small clouds dragged by the wind, dynamically decoupled from the ionized gas traced by $H\alpha$ emission, but almost equally energetically important.

The analysis of the behavior of the derived G_0 along the minor axis of M 82 can help test this hypothesis. In Fig. 20 we show the values of G_0 we have obtained from the PDR modeling along the minor axis of the galaxy as a function of the distance from the galaxy's center, for the different input data sets we have used. The two panels show the cut for the southern (left) and the northern (right) outflow.

We compare these values to the ISRF values provided by the starburst assuming pure geometrical dilution without any extinction. This corresponds to the maximum possible contribution of the starburst light in the outflow. In order to calculate it we assume the following: 1) the starburst has a diameter of 500 pc (Förster-Schreiber et al. 2003), which corresponds to $\sim 30''$, and therefore we consider only the points at distances $\geq 15''$, along the minor axis on each side; 2) the ISRF at this distance in both cones of the outflow, is equal to what we have calculated from the PDR modeling at the same distance. The resulting values are indicated with the blue solid line in both panels of Fig. 20. This figure shows that the ISRF values derived from the PDR modeling agree within the uncertainties with the blue line, except for the G_0 values obtained by using as input to the PDR models the [CII] corrected from the ionized gas contribution for a density equal to 15 cm^{-3} , which is a rather extreme case. Agreement with the maximum G_0 obtained by neglecting extinction would indicate that most of the starburst FUV photons can travel the outflow, with a low probability of being absorbed. Since we know that there is dust in the outflow, the only way this can happen is that there are big dust-free holes or, in other words, that most of the existing dust must be concentrated in clouds with low filling factors. This supports the cloudlets interpretation we have proposed above and it also shows that the starburst light is sufficient to heat most of these cloudlets and that no significant extra heating (i.e. in situ star formation) is required.

We have already discussed in Sect. 3.6 that the ionized gas traced by the [OIII] line at $88 \mu\text{m}$ and that traced by the $H\alpha$ emission are not kinematically coupled and probably not even co-spatial in the outflow. We have also shown evidences that these two lines likely trace gas ionized by two different physical processes: the $H\alpha$ emission arises from a combination of photoionization by the starburst and shocks: the first process dominates the emission towards the outflow axis, the second process traces predominantly the gas shocked when the hot flowing plasma encounters the halo, and it is therefore more confined in the outflow walls. The [OIII] $88 \mu\text{m}$ emission is more concentrated along the minor axis of the galaxy and it is most likely dominated by photoionization. Taking also into account that the [OIII] $88 \mu\text{m}$ emitting gas flows at the same velocity of the neutral atomic gas, we

propose that this is gas surrounding the PDR-molecular cloudlets ionized by the starburst light. This ionized component though is more collimated than the neutral gas component, suggesting that the ionized gas associated with the PDR clouds, is decreasing towards the periphery of the outflowing material. This is probably due to the fact that the number of UV photons necessary to excite the [OIII] line ($>35.12 \text{ eV}$) directly emitted from the starburst decreases faster than the number of the less energetic UV photons necessary to excite the [OI] and [CII], as the length of the material they have to pass through increases.

Finally, there is yet a third component of material entrained in the outflow: that of the dust detected through the polarization of the visible light reported by Yoshida et al. (2011). This dust, which scatters the nuclear visible light, is made by grains larger and hence heavier than PAHs. In fact their velocity is lower ($\sim 10 \text{ km s}^{-1}$ at 1 kpc distance above the galaxy's disk) than that observed for the PDR component associated with the cold gas and presumably with PAHs.

4.4.2. What powers the outflow in M 82?

In this Section we try to establish whether the radiation pressure or/and the mechanical energy due to the supernovae explosion is powering the PDR component participating to the motion in the outflow of M 82 and whether the outflow is energy or momentum driven (i.e. whether they conserve the energy or the momentum).

The momentum rate provided by supernovae explosion can be calculated following equation 10 from Murray et al. (2005):

$$\dot{P}_{\text{SN}} \sim 2 \times 10^{33} \left(\frac{\text{SFR}}{1 M_{\odot} \text{ yr}^{-1}} \right) \text{ g cm s}^{-2}. \quad (6)$$

This assumes a supernovae rate $\nu_{\text{SN}} = 0.01 \text{ yr}^{-1}$ for a SFR equal to $1 M_{\odot} \text{ yr}^{-1}$. Förster-Schreiber et al. (2003) have calculated that the supernovae rate in M 82 is 0.13 yr^{-1} and that the SFRs of the two starburst episodes at their peak are equal to 18.5 and $6.3 M_{\odot} \text{ yr}^{-1}$ giving a total SFR of $24.8 M_{\odot} \text{ yr}^{-1}$. A supernovae rate of 0.01 yr^{-1} for a SFR equal to $1 M_{\odot} \text{ yr}^{-1}$ corresponds to a supernovae rate of ~ 0.25 per a SFR of $24.8 M_{\odot} \text{ yr}^{-1}$, which is a factor of 2 higher than what found in M 82. This means that we have to divide Eq. (6) by 2. The total momentum rate available from the SN explosion is then $\sim 2.5 \times 10^{34} \text{ g cm s}^{-2}$.

The momentum rate given by the radiation pressure is L_{SB}/c , assuming that the optical depth at the base of the outflow is 1. The total bolometric starburst luminosity of M 82 is $6.6 \times 10^{10} L_{\odot}$ (Förster-Schreiber et al. 2003), which gives a radiation pressure momentum rate equal to $8.5 \times 10^{33} \text{ g cm s}^{-2}$, a factor of 3 less than mechanical momentum rate.

The observed momentum rate for both cones of the outflow ($\dot{M}_{\odot} \times v_{\text{deproj}} \text{ g cm s}^{-2}$) ranges from 5 to $12 \times 10^{33} \text{ g cm s}^{-2}$, depending on the input data set (see Table 2).

The energy rate due to supernovae explosion under the same assumptions of Eq. (6) is (Eq. (34) of Murray et al. 2005):

$$\dot{E}_{\text{SN}} \sim 3 \times 10^{40} * \left(\frac{\text{SFR}}{1 M_{\odot} \text{ yr}^{-1}} \right) \text{ g cm s}^{-2} \quad (7)$$

which for M 82 translates in an energy rate $\sim 3.7 \times 10^{41} \text{ erg s}^{-1}$.

The observed energy rate carried by the atomic PDR component in the outflow of M 82 ($\frac{1}{2} \dot{M}_{\text{deproj}}^2$) ranges from $2-5 \times 10^{40} \text{ erg s}^{-1}$.

The momentum and energy rates in the outflow carried by the cold molecular component are equal to $21 \times 10^{33} \text{ g cm s}^{-2}$

Table 4. Available and observed molecular and atomic gas energetics in the outflow of M 82.

Momentum rates	Available $10^{33} \text{ g cm s}^{-2}$		Used $10^{33} \text{ g cm s}^{-2}$
\dot{P}_{SN}	25	$\dot{P}_{\text{molecular}}$	21
\dot{P}_{SB}	8.5	\dot{P}_{atomic}	5–12
		$\dot{P}_{\text{H}\alpha}$	2
total	33.5		28–35
Energy rates	Available 10^{40} g s^{-1}		Used 10^{40} g s^{-1}
\dot{E}_{SN}	37	$\dot{E}_{\text{molecular}}$	10
		\dot{E}_{atomic}	2–5
		$\dot{E}_{\text{H}\alpha}$	40
Total	37		52–55

and $10^{41} \text{ erg s}^{-1}$ respectively, assuming a deprojected molecular velocity of 100 km s^{-1} and a dynamical time equal to 10^7 yr (Walter et al. 2002). We have seen in the previous section that the cold molecular component traced by the CO emission is likely to be dynamically coupled to the neutral atomic gas PDR component. Under this assumption we can add the energetics of these two components to estimate a total balance between the momentum (energy) available and those observed to move this material in the outflow. We obtained a total observed momentum rate $\dot{P}_{\text{atomic}} + \dot{P}_{\text{molecular}} \sim 26\text{--}33 \times 10^{33} \text{ g cm s}^{-2}$ and an observed energy deposition rate equal to $\dot{E}_{\text{atomic}} + \dot{E}_{\text{molecular}} \sim 12\text{--}15 \times 10^{40} \text{ erg s}^{-1}$ to be compared with the total momentum and mechanical energy deposition rates available of $\sim 34 \times 10^{33} \text{ g cm s}^{-2}$ and $\sim 37 \times 10^{40} \text{ erg s}^{-1}$ respectively.

Table 4 summarizes these values: on the left it lists the momentum (energy) rate available in the system and on the right the observed momentum (energy) rates in M 82. Both the total momentum and energy deposition rates available in the system are comparable to the observed values. The momentum driven outflow is not compatible with the observations if the source of power is the radiation pressure alone. The energy driven case seems to leave more room for agreement between the observed and the available energy of the PDR outflowing material.

However, if we include in the energy and momentum budget calculation also the numbers necessary to sustain the outflowing material observed in H α by Shopbell & Bland-Hawthorn (1998) the energy driven case becomes only marginally compatible with the observations. In fact, assuming a mass of the outflow observed at these wavelengths equal to $5.8 \times 10^6 M_{\odot}$, a kinetic energy equal to $2.0 \times 10^{55} \text{ erg}$, a mean deprojected velocity of $\sim 600 \text{ km s}^{-1}$ (Shopbell & Bland-Hawthorn 1998) and a length of the outflow above the galactic plane equal to 1 kpc, one derives a momentum rate $\sim 2.2 \times 10^{33} \text{ g cm s}^{-2}$ and an energy rate $\sim 40 \times 10^{40} \text{ erg s}^{-1}$ (also listed in Table 4). Taking into account the overall uncertainties (\sim a factor of 2) of the numbers derived from the above calculation and considering the cold molecular gas, the neutral atomic gas and hot ionized gas phases energetic together, we conclude that, assuming a simple jet-like outflow geometry, both the energy and momentum driven process are compatible with the observed values, although the momentum driven case seems to be slightly favored.

4.5. Line diagnostic diagrams

Figure 21 shows the ratio of each of the observed lines to the FIR continuum as well as the [OI] $63 \mu\text{m}$ /[CII], and [OIII]/[OI] $63 \mu\text{m}$ ratios as a function of the $F_{[60 \mu\text{m}]} / F_{[100 \mu\text{m}]}$

ratio, equivalent to the IRAS colors, derived from our PACS maps. The latter traces the dust temperature and therefore, to first order also the interstellar radiation field. The M 82 values are shown in gray scale. Overplotted are the data collected from the literature or measured in the PACS GT Key Program SHINING (Graciá Carpio et al. 2011). Different symbols refer to different galaxy types (see figure caption for details). The emission line data points of M 82 are those derived from the final maps reduced to the same spatial resolutions. The maps at $60 \mu\text{m}$ and $100 \mu\text{m}$ have been derived as explained in Sect. 4.1.1.

There is excellent agreement between the M 82 data, which probe regions of linear extent of $\sim 300 \text{ pc}$, and the global emission properties of galaxies. This means that the physical mechanisms governing the observed relationships act up to a scale as small as 300 pc , and they are the same independent on whether they act in the starburst region, the diffuse disk or the outflow. The only difference is in the panel showing the [OI] $63 \mu\text{m}$ /FIR ratio that in the case of M 82 is remarkably constant, while the galaxy sample is exhibiting a large scatter. It is interesting to note that the scale we probe ($\sim 300 \text{ pc}$) is comparable to the upper limit of the scale where the Kennicutt-Smith law begins to break (Schruba et al. 2010).

Each left and middle panel of Fig. 22 shows the $F_{\text{IRline}} / F_{\text{IRcontinuum}}$ ratios versus the $F_{[60 \mu\text{m}]} / F_{[100 \mu\text{m}]}$ colors and the FIR luminosities for M 82 only, color coded depending on whether the regions belong to the outflow, the starburst or the disk of M 82 as shown in the upper panel of Fig. 18. The top panels show the [CII]/FIR ratio decreases by one order of magnitude with the increase of the $F_{[60 \mu\text{m}]} / F_{[100 \mu\text{m}]}$ IRAS color and the FIR luminosity, nicely following the decreasing trend outlined from the whole SHINING galaxy sample (Graciá Carpio et al. 2011). As expected, the lowest [CII]/FIR values in M 82 arise from the starburst region (green points). This decrease was first discovered with the ISO LWS and it has been referred to as the [CII]-deficit (Fischer et al. 1999, 2001; Maloitra et al. 2001; Luhman et al. 1998, 2003; Abel et al. 2009), i.e. the warmer, more active and more infrared luminous the systems are, the less [CII] with respect to their FIR emission they emit.

The near universality of the [CII] deficit for luminous systems has been recently challenged by observations of high redshift galaxies, which show a “normal” [CII]/FIR ratio despite of their high FIR luminosities (Maiolino et al. 2009; Hailey-Dunsheath et al. 2010; Ivison et al. 2010; Stacey et al. 2010; Wagg et al. 2010; Sturm et al. 2010). On the other hand, if the [CII]/FIR ratio is plotted against the ratio between the FIR luminosity and the H $_2$ molecular mass, rather than FIR luminosities, the scatter in the relation is significantly reduced as is the disparity between systems at low and high redshift. This means that the [CII] deficit becomes universal at all redshifts above a threshold of the $L_{\text{FIR}} / M_{\text{H}_2}$ ratio, a commonly used indicator of star formation efficiency or evolutionary stage (González-Alfonso et al. 2008; Graciá Carpio et al. 2011). Furthermore, Graciá Carpio et al. find that this deficit extends to other PDR and pure HII region FIR lines (see their Fig. 2). In galaxies where L_{FIR} is predominantly powered by star formation, the $L_{\text{FIR}} / M_{\text{H}_2}$ ratio is, to first approximation, the ratio between the energy released by the star formation and the gas reservoir from where the stars form and therefore it is a parameter directly related to the star formation efficiency. This is not the case for the L_{FIR} . Graciá Carpio et al. (2011) show that above a certain $L_{\text{FIR}} / M_{\text{H}_2}$ threshold one also finds an increase of the ionization parameter U , i.e. the ratio between the ionizing photons to the gas density at the inner surface of the ionized cloud. The higher this parameter is the larger the

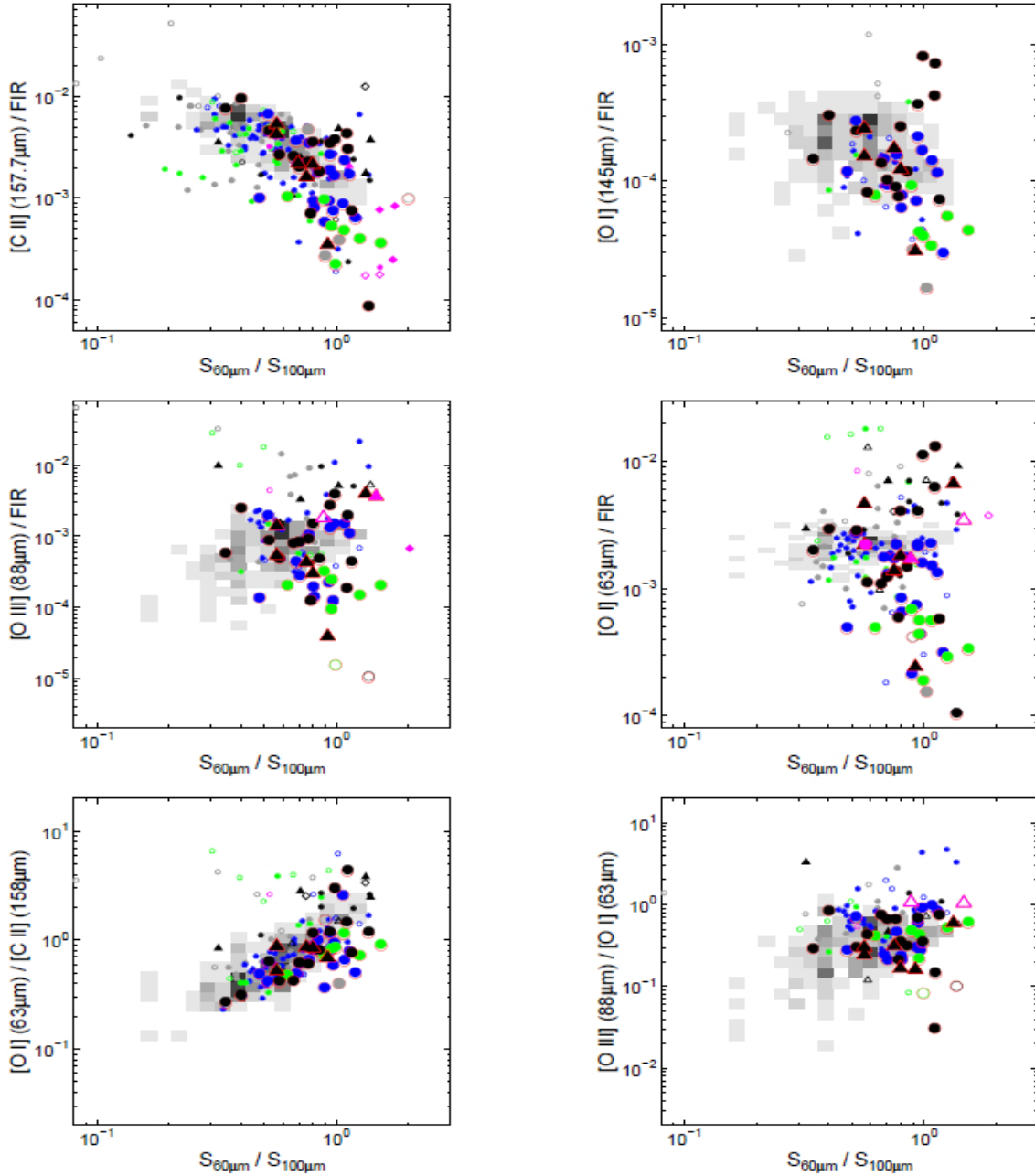


Fig. 21. [CII]/FIR, [OI] 145 μm /FIR, [OIII]/FIR, [OI] 63 μm /FIR, [OI] 63 μm /[CII] and [OIII] 88/[OI] 63 μm versus the continuum 60/100 μm ratio. M 82 values are shown as gray scale. Symbols are the following (Graciá Carpio et al. 2011, and in prep.): big symbols: SHINING/PACS observations; filled symbols: the lines are detected; open symbols: one or both lines are not detected; blue points: HII galaxies; green points: LINER galaxies; black symbols: AGNs; circles: Seyfert 2 galaxies; triangles: Seyfert 1 galaxies; diamonds: QSOs; magenta points: high- z galaxies; grey points: unclassified galaxies; small magenta points: flux at 25 or at 100 μm is an upper limit. (This figure is available in color in the electronic form.)

HII region and the FIR emitted by the dust heated in the HII region. This increasing FIR does not mean a corresponding increase in the FIR emission lines arising from the PDR, thus the global $FIR(PDR)_{\text{line}}/FIR(\text{HII} + PDR)_{\text{continuum}}$ ratio decreases. The values of the $L_{\text{FIR}}/M_{\text{H}_2}$ threshold ($>80 L_{\odot} M_{\odot}^{-1}$) is very close to the threshold above which the star formation becomes much more efficient than what is predicted by the Kennicutt-Schmidt relation for normal star forming galaxies (Genzel et al. 2010). This similarity suggests that the galaxies and the regions within galaxies which exhibit a FIR_{line} deficit, are in this highly efficient mode of star formation.

In order to determine in which mode of star formation the various regions of M 82 are, we want to plot the line/FIR ratios of the points belonging to M 82 as a function of $L_{\text{FIR}}/M_{\text{H}_2}$. Since we do not have a CO map of M 82 available from which we can derive the H_2 mass, we use instead the mass of the PDR gas to calculate the $L_{\text{FIR}}/M_{[\text{CII}](\text{H})}$ ratio. The cold molecular gas is more closely related to the site of star formation than the atomic neutral gas, but the atomic gas we are considering here is that associated with the PDR and therefore it is also related to the star formation, although not as directly as the molecular gas. This is why the ratio between the FIR luminosity and the mass of

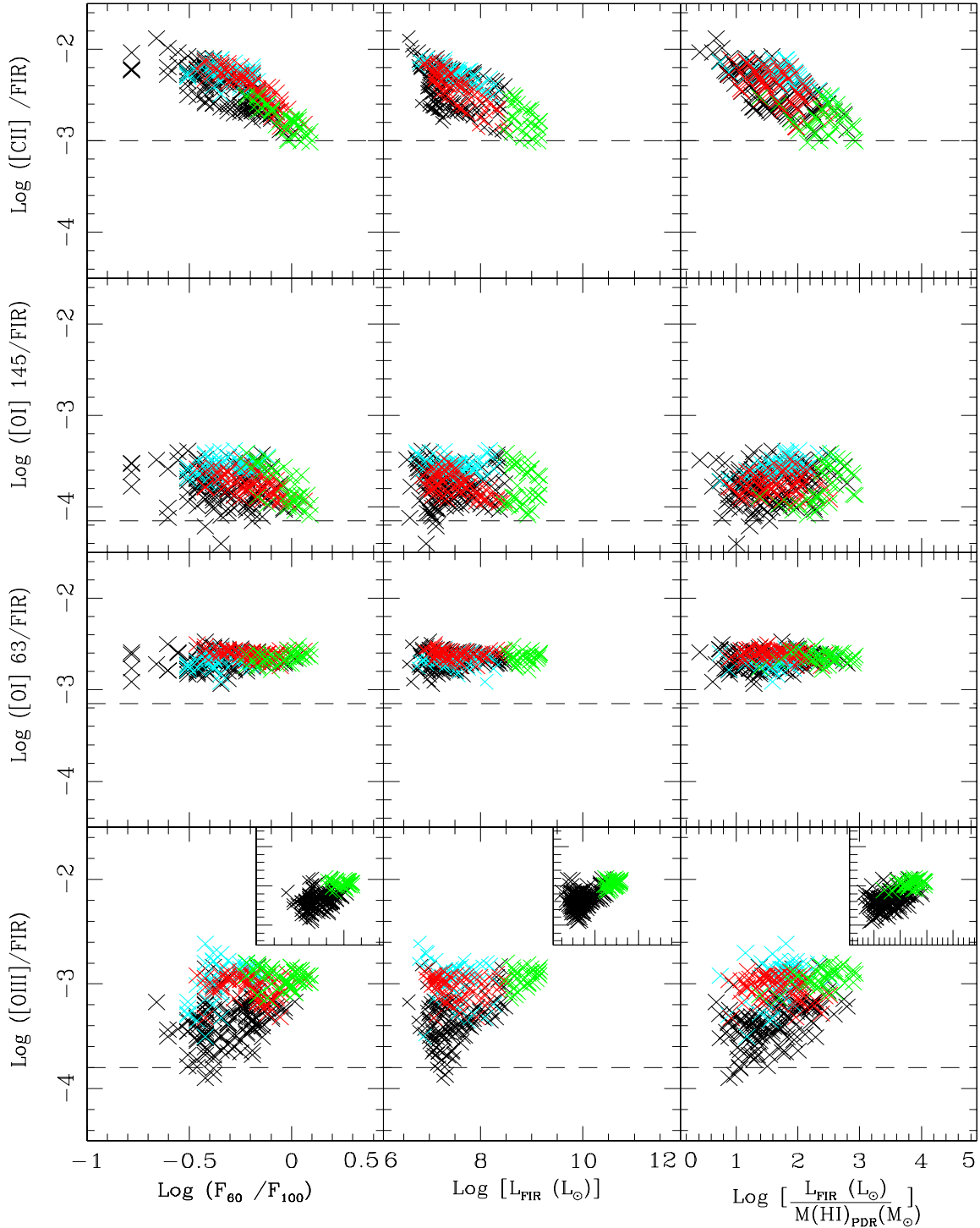


Fig. 22. The line/FIR ratio versus: *left*: 60/100 colors; *middle*: L_{FIR} ; *right*: $L_{\text{FIR}}/M(\text{HI})_{\text{PDRs}}$. Data are for M 82 only. Black points are from the diffuse disk; red points from the southern outflow; cyan points from the northern outflow and green points from the starburst. The small frames in the last row show the same relation reported in the big frames but only for the points belonging to the disk (black) and the starburst (green). The horizontal lines correspond to the threshold identified by Graciá Carpio et al. (2011) between galaxy with normal (above) and deficient (below) $FIR_{\text{line}}/FIR_{\text{continuum}}$ ratios, or between normal and high efficiency of SF. (This figure is available in color in the electronic form.)

neutral hydrogen associated with the PDRs can be considered to first order, as star formation efficiency.

We have produced plots analogous to the $FIR_{\text{line}}/FIR_{\text{continuum}}$ deficit diagrams shown in Graciá Carpio et al. (2011) for M 82 (color coded: disk in black, starburst in green, north outflow in cyan and south outflow in red, see also the schematic figure on top right of Fig. 18). These diagrams are shown in the right panels of Fig. 22 for each line. We have

also plotted the horizontal lines that Graciá Carpio et al. (2011) consider as the limit between galaxy with normal and deficient $FIR_{\text{line}}/FIR_{\text{continuum}}$ ratios.

The first thing to notice is that even the starburst region of M 82 is not in this high efficiency mode of star formation, since all points are above the horizontal lines. Nevertheless we observe different behaviors among the different lines.

The [CII]/FIR ratio gently decreases in all cases, even when plotted as function of the $L_{\text{FIR}}/M_{\text{[CII]}}(H)$, whereas the similar plot in Graciá Carpio et al. (2011) who used the mass of H_2 , shows an almost constant behavior up to ($\sim 80 L_{\odot} M_{\odot}^{-1}$), and then a decrease. However, we notice that the data shown in Graciá Carpio (2011) did not include the whole SHINING sample³ and the data available at that time contained more ULIRGs/AGNs than starbursts and star forming galaxies. Now that the sample is complete and more starbursts/star forming galaxies populate the low L_{FIR}/M_{H_2} part of the plot, a decrease at low L_{FIR}/M_{H_2} is also clearly visible for the SHINING sample (Graciá Carpio et al., in prep.) although with a slope much less steep than that followed by galaxies at $L_{\text{FIR}}/M_{H_2} > 80$. This continuous decrease is predicted by models which assume an increasing production of FIR emission arising by the dust heated in the HII regions, as the ionization parameter U increases (see Fig. 12 of Abel et al. 2009).

The [OI] 63 μm /FIR and the [OI] 145 μm /FIR ratios in M 82 are remarkably constant and, in contrast to the [CII]/FIR behavior, do not show any hint of decline in M 82. The constancy is compatible with what is observed in the whole SHINING sample, which shows a decline of the [OI]/FIR ratio only at 60/100 ratios higher than that probed in M 82.

Both trends can be understood by modeling these ratios with CLOUDY as shown in Fig. 3 of Graciá Carpio et al. (2011). These figures show the FIR_{line}/FIR ratios on diagrams of the ionization parameter U versus the gas density n_H . Each diagram is divided into gray and red zones, corresponding to the typical values of starburst/star forming galaxies and ULIRGs respectively. The loci of the line over FIR value corresponding to the transition between the zones correspond to the horizontal lines shown in Fig. 22. First we address the diagrams involving only the PDR lines ([CII], and the two [OI] lines): when moving diagonally on these diagram, increasing both parameters, the [CII]/FIR ratio decreases but the [OI]/FIR ratios do not change significantly because in the first case one moves perpendicular to the loci of constant [CII]/FIR and in the second case one moves almost parallel to the loci of constant [OI]/FIR, at least in the range of line/FIR ratios spanned by M 82 and starbursts in general (gray zones in Fig. 3 of Graciá Carpio et al. 2011). The behavior of the lines arising from ionized gas is reversed with respect to what we have just examined in the case of PDR lines. In particular we concentrate here on the [OIII]/FIR line loci, on the $U-n_H$ diagram. We can see that in this case, increasing both parameters means increasing the HII-line/FIR ratio, as it is observed in M 82 shown in the bottom panel of Fig. 22. However, it is worth mentioning that the pure HII region lines are very sensitive to the input SED used for the modeling, and in particular to the hardness of the exciting photons, much more than the lines originating from PDRs or the dust temperature and total flux which is sensitive to the energy of the heating photons rather than to the hardness.

From the $U-n_H$ diagram we can derive the $FIR_{\text{line}}/FIR_{\text{continuum}}$ ratios expected for the values calculated by Förster Schreiber et al. (2001) for M 82 ($U = -2.3$ dex and $n_e \sim n_H = 300 \text{ cm}^{-3}$). These values agree well to the averaged values we observe, as shown by the green crosses in all panels of Fig. 22.

Finally, a closer look to the trend followed by the [OIII]/FIR ratio in Fig. 22 seems to suggest that there exist two different behaviors in M 82. In the disk (black points) and in the starburst (green points) this ratio increases with IRAS color,

FIR luminosity and L_{FIR}/M_{H_2} as expected (see inner panels in the bottom row in Fig. 22). On the other hand, in the outflow this ratio remains constant and is higher than the corresponding point of the disk at low IRAS color, FIR emission and L_{FIR}/M_{H_2} ratios. This suggests that in the outflow the [OIII] is enhanced with respect to the FIR emission. We have seen that the [OIII] emission in the outflow is dynamically coupled with the gas emitting in the [CII] and [OI] lines, that we have associated to PDR clouds. We have also seen that the PDRs in the outflow survive in form of small cloudlets. We can imagine that the dust associated with these small clouds is shielded from the UV photons resulting in colder FIR colors and lower FIR emission. We notice that shocks do not play a significant role in the heating of the PDR material anywhere in M 82 including the outflow, since the [OI] 63 μm / [CII] ratio is always well below the values (~ 10) predicted in the presence of shocks (Hollenbach & McKee 1989).

5. Summary and conclusions

We have mapped a $2.5' \times 2.5'$ region of M 82 in four FIR atomic fine-structure lines, [CII] at 158 μm , [OI] at 63 and 145 μm and [OIII] at 88 μm , with the PACS spectrometer on board the *Herschel* Space Observatory, reaching unprecedented spatial resolution ($\sim 200\text{--}300$ pc) at these wavelengths. The mapped area covers approximately 1 kpc along the minor axis of the galaxy. This enables detection of the M 82 outflow structures in these lines for the first time. Since the [CII] and [OI] lines are the main coolants of the cold neutral medium, these observations trace and probe the atomic gas in the outflow. This paper presents the first analysis of these observations with emphasis on the nature and structure of the atomic gas in the outflow and on its relation with other ISM phases studied in previous works. We summarize the main results as follows.

- We derived intensity, radial velocity and dispersion maps of the entire mapped region in all lines. We also used the offline continuum images and the parallel array scans to produce a dust temperature map. The line dispersion maps most clearly show two dynamically separated structures, disk and outflow, since the dispersion in the outflow is $\sim 50\text{--}100 \text{ km s}^{-1}$ higher than that in the disk. These distinct components are also visible in the radial velocity maps and indicate that the northern outflow is receding from us while the southern outflow is moving toward us, in agreement with previous results. In the outflow, the mean deprojected velocity, calculated assuming a simply inclined jet-like geometry, is $\sim 75 \text{ km s}^{-1}$ for both the cold neutral and the ionized gas traced by the [OIII] 88 μm line, close to the average velocity of the molecular gas ($\sim 100 \text{ km s}^{-1}$) reported by Walter et al. (2002) and much smaller than the velocity of the outflowing material observed in $H\alpha$ ($\sim 600 \text{ km s}^{-1}$, Shopbell & Bland-Hawthorn 1998).
- Analysis of the line ratio maps and of the line-to-continuum maps confirms earlier findings that the base of the northern outflow is more obscured than the southern one due to the inclination of the galaxy disk. These maps also reveal that the opening angle of the cold gas component of the outflow is much larger than the ionized gas traced by the [OIII] 88 μm which appears much more collimated.
- We have carried out PDR modeling of the neutral gas emission lines to derive the key physical parameters of the atomic gas within and surrounding the starburst, stellar disk and the outflow components of M 82. By applying the Kaufman et al. (1999) PDR models to each pixel of our line intensity images we were able to produce, for the first time in an external

³ The SHINING sample, P.I. E. Sturm, includes 50 galaxies ranging from HII, starbursts, Seyfert1 and Seyfert2, and LINERs and including LIRGs and ULIRGs, Graciá Carpio et al. (in prep.)

galaxy, maps of the FUV interstellar radiation field G_0 , the gas density n_{H} , the gas temperature T_{gas} , the atomic gas cloud beam filling factor, the column density of atomic hydrogen, and the [CII] opacity. Since the correction for the contribution of [CII] emission from ionized gas is very uncertain we run the model with and without it, but the resulting maps do not differ significantly. Solution maps using each [OI] line together with the [CII] and continuum TIR emission were similar to within the errors for all parameters except the gas density, probably because of alignment problems between the [OI] 63 μm and [CII] map. For this reason and also because the [OI] 63 μm optical depth can vary significantly in the galaxy we based our analysis only on the results obtained using as input to the model the [OI] line at 145 μm together with [CII] and TIR. The area beam filling factor decreases by up to an order of magnitude in the diffuse disk and in the outflow. G_0 and n_{H} both vary from ~ 50 to few 10^3 and the atomic gas temperatures are in the range of 300–400 °K. The [CII] optical depth is everywhere much less than unity, enhanced along the disk but decreasing toward the starburst region, perhaps because some material has been cleared out by the winds that power the outflow.

- The relation between G_0 and n_{H} in M 82 is the same as has been observed in previous works for the global emission of star forming galaxies extended by almost two orders of magnitude towards smaller values. In this plot, the same relation is followed regardless of whether the points belong to the starburst, the outflow or the diffuse disk, confirming that the clouds in the outflow are still organized in PDRs very similar to the clouds in the rest of the galaxy.
- We find that the mass and the kinetic energy of the outflowing cold neutral gas are $\geq 2-8 \times 10^7 M_{\odot}$ and $\geq 1-5 \times 10^{54}$ erg slightly smaller than the corresponding values found for the outflowing molecular gas ($\sim 3.3 \times 10^8 M_{\odot}$, $\sim 3 \times 10^{55}$ erg). The mass outflow rate of the molecular and atomic gas is $\sim 43-58 M_{\odot} \text{ yr}^{-1}$ comparable to the SFR of M 82 equal to $25 M_{\odot} \text{ yr}^{-1}$, resulting in a mass loading factor $\dot{M}/\text{SFR} \sim 2$. This result, together with the fact that these two components show similar velocities, suggests that they are dynamically coupled with similar origin. Since the cold atomic gas is consistent with emission from classical PDRs (i.e. interface regions between the ionized and molecular gas) with small filling factors, the coupling of these two cold components of the ISM is naturally explained if both the molecular and atomic media belong to the same disk clouds entrained in the outflow by the wind where they partially evaporate due to heating driven by thermal conduction from the hot gas, surviving as clouds smaller than their original size. This scenario is supported by the fact that the decline of the derived FUV ISRF in the outflow is consistent with a pure geometrical dilution, indicating that FUV photons can travel in the outflow with a low probability of being absorbed by dust, which therefore must be concentrated in small clouds. This also implies that in the outflow, there is no need for a significant in situ star formation in addition to the starburst light.
- We have found that in the outflow, the ionized gas traced by the FIR [OIII] 88 μm line flows at a much smaller velocity ($\sim 75 \text{ km s}^{-1}$) than the ionized gas traced by the $\text{H}\alpha$ emission ($\sim 600 \text{ km s}^{-1}$, Shopbell & Bland-Hawthorn 1998) but at a velocity similar to that of the neutral atomic gas traced by the [CII] and [OI] lines. We have also not found line splitting in any of the observed FIR lines, including the [OIII] line at 88 μm , despite the fact that the line splitting detected in $\text{H}\alpha$ is large enough to be detected at the PACS

spectral resolution. These results suggest that [OIII] 88 μm and $\text{H}\alpha$ line emission trace two different ionized gas components, both in velocity and in physical space. We propose a scenario in which the bulk of the [OIII] line at 88 μm traces gas surrounding the PDR cloudlets observed in the [CII] and [OI] lines, photoionized by the starburst radiation. This would justify the fact that all these components flow at the same velocity. In this scenario, the bulk of the $\text{H}\alpha$ emission arises from the shocked gas at the interface between the hot plasma wind emitting in X-ray and the halo. This would explain why the $\text{H}\alpha$ emission is mainly located in the walls of the outflow as demonstrated by the observed line splitting.

- The momentum and the energy available to drive the outflowing gas, molecular atomic and ionized, are both compatible with that observed in the flows, although the momentum driven case seems to be slightly favored by the data.
- We compare the trends found in the relative FIR fine-structure line fluxes as a function of the IRAS 60/100 colors of normal and infrared-bright galaxies to those found in the spatially resolved, ~ 300 pc regions of M 82. We find that for all but the warmest far-infrared colors of ULIRGs and the most extreme LIRGs, the ratios in M 82 overlap with the trends found recently by Graciá Carpio et al. (2011) for the whole galaxies. These authors explore parameter space in density and ionization parameter. Based on photoionization models, they argue that the atomic fine-structure line deficits found in the neutral gas of galaxies with the warmest FIR colors and the highest values of $L_{\text{FIR}}/M_{\text{H}_2}$ are caused by the presence of high ionization parameters in which the dust rather than the gas absorbs most of the ionizing photons. They suggest that these most extreme galaxies are in the high efficiency mode of star formation rather than in a normal/Milky Way-like mode of star formation. Importantly we find that down to 300 pc size regions, even in regions of the highest star formation efficiency in M 82, only the normal mode of star formation is present, i.e. no hint of bimodality is found.

Acknowledgements. PACS has been developed by a consortium of institutes led by MPE (Germany) and including UVIE (Austria); KU Leuven, CSL, IMEC (Belgium); CEA, LAM (France); MPIA (Germany); INAF-IFSI/OAA/OAP/OAT, LENS, SISSA (Italy); IAC (Spain). This development has been supported by the funding agencies BMVIT (Austria), ESA-PRODEX (Belgium), CEA/CNRS (France), DLR (Germany), ASI/INAF (Italy), and CICYT/MCYT (Spain). Basic research in IR astronomy at NRL is funded by the US ONR; J.F. also acknowledges support from the NHSC. E.G.-A. thanks the support by the Spanish Ministerio de Ciencia e Innovación under project AYA2010-21697-C05-01, and is a Research Associate at the Harvard-Smithsonian Center for Astrophysics.

References

- Aalto, S., Garcia-Burillo S., Muller S., et al. 2011, A&A, 537, A44
 Abel, N. P. 2006, MNRAS, 368, 1949
 Abel, N. P., Dudley, C., Fischer, J., et al. 2009, ApJ, 701, 1147
 Alton, P. B., Davies, J. I., & Bianchi, S. 1999, A&A, 343, 51
 Brauer, J. R., Dale, D. A., & Helou, G. 2008, ApJS, 178, 280
 Calzetti, D., Kinney, A. L., & Storchi-Bergmann, T. 1994, ApJ, 429, 582
 Chung, A., Yun, M. S., Narayanan, G., et al. 2011, ApJ, 732, 15
 Chynoweth, K. M., Langston, G. I., Yun, M. S., et al. 2008, AJ, 135, 1983
 Cicone, C., Feruglio C., Maiolino R., et al. 2012, A&A, 534, A99
 Colbert, J. W., Malkan, M. A., Clegg, P. E., et al. 1999, ApJ, 511, 721
 Cooper, J. L., Bicknell, G. V., Sutherland, R. S., et al. 2008, ApJ, 674, 157
 Crawford, M. K., Genzel, R., Townes, C. H., et al. 1985, ApJ, 291, 755
 Croton, D. 2006, MNRAS, 369, 1808
 Croxall, K. V., Smith, J. D., Wolfire, M., et al. 2012, ApJ, 747, 81
 Dale, D. A., Helou, G., Contursi, A., et al. 2001, ApJ, 549, 215
 Dietz, R. D., Smith, J., Hackwell, J. A., et al. 1986, AJ, 91, 758
 Engelbracht, C. W., Kundurthy, P., Gordon, K. D., et al. 2006, ApJ, 642, L127

- Feruglio, C., Maiolino, R., Piconcelli, E., et al. 2010, *A&A*, 518, L155
- Finkelstein, S. L., Cohen, S. H., Windhorst, R. A., et al. 2011, *ApJ*, 735, 5
- Fischer, J., Lord, S. D., Unger, S. J., et al. 1999, *ESA-SP*, 427, 817
- Fischer, J., Sturm, E., González-Alfonso, E., et al. 2010, *A&A*, 518, A41
- Fischer, J., Allen, R., Dudley, C. C., et al. 2011, in *Spectroscopic Challenges of Photoionized Plasmas*, eds. G. Ferland, & D. W. Savin, *ASP Conf. Ser.*, 247
- Förster Schreiber, N. M., Genzel, R., Lutz, D., et al. 2001, *ApJ*, 552, 544
- Förster Schreiber, N. M., Genzel, R., Lutz, D., et al. 2003, *ApJ*, 599, 193
- Freedman, W. L., Hughes, S. M., Madore, B. F., et al. 1994, *ApJ*, 427, 628
- Fruchter, A. S., & Hook, R. N. 2002, *PASP*, 114, 144
- Gebhardt, K., Bender, R., Bower, G., et al. 2000, *ApJ*, 539, L13
- Genzel, R., Tacconi, L. J., & Graciá-Carpio, J. 2010, *MNRAS*, 407, 209
- González-Alfonso, E., Smith, H. A., Ashby, M. L. N., et al. 2008, *ApJ*, 675, 303
- Graciá Carpio, J., Sturm, E., Hailey-Dunsheath, S., et al. 2011, *ApJ*, 728, L7
- Greve, A. 2004, *A&A*, 416, 67
- Griffiths, R. E., Ptak, A., Feigelson, E. D., et al. 2000, *Science*, 290, 1325
- Gültekin, K., Richstone, D. O., Gebhardt, K., et al. 2009, *ApJ*, 698, 198
- Hailey-Dunsheath, S., Nikola, T., Stacey, G. J., et al. 2010, *ApJ*, 714, L162
- Heckman, T. M., Armus, L., & Miley, G. K. 1990, *ApJS*, 74, 833
- Heckman, T. M. 1998, in *Starbursts: Lessons for the Origin and Evolution of Galaxies and the Intergalactic Medium*, eds. C. E. Woodward, J. M. Shull, & H. A. Thronson Jr., *ASP Conf. Ser.*, 148
- Helou, G., Khan, I. R., Malek, L., et al. 1988, *ApJS*, 68, 151
- Hollenbach, D. J., & McKee, C. F. 1989, *ApJ*, 342, 306
- Hollenbach, D. J., & Tielens, A. G. G. M. 1999, *Rev. Mod. Phys.*, 71, 173
- Hoopes, C. G., Heckman, T. M., Strickland, D. K., et al. 2005, *ApJ*, 619, L99
- Iverson, R. J., Swinbank, A. M., Swinyard, B., et al. 2010, *A&A*, 518, L35
- Kaneda, H., Ishihara, D., Suzuki, T., et al. 2010, *A&A*, 514, A14
- Kaufman, M. J., Wolfire, M. G., Hollenbach, D. J., et al. 1999, *ApJ*, 527, 795
- Kennicutt, R. C., Jr. 1998, *ARA&A*, 36, 189
- Leeuw, L. L., & Robson, E. I. 2009, *AJ*, 137, 517
- Lehnert, M. D., & Heckman, T. M. 1995, *ApJS*, 97, 89
- Lloyd, C., 2003, *ESASP*, 482, 399
- Luhman, M. L., Satyapal, S., Fischer, J., et al. 1998, *ApJ*, 504, L11
- Luhman, M. L., Satyapal, S., Fischer, J., et al. 2003, *ApJ*, 594, 758
- Maiolino, R., Caselli, P., Nagao, T., et al. 2009, *A&A*, 500, L1
- Malhotra, S., Kaufman, M. J., Hollenbach, D., et al. 2001, *ApJ*, 561, 766
- McKeith, C. D., Greve, A., & Downes, D. 1995, *A&A*, 293, 703
- Melo, V. P., Muñoz-Tuñón, C., Maíz-Apellániz, J., et al. 2005, *ApJ*, 619, 270
- Merritt, D., & Ferrarese, L. 2001, *MNRAS*, 320, L30
- Micelotta, E. R., Jones, A. P., & Tielens, A. G. G. M. 2010, *A&A*, 510, A37
- Magorrian, J., Tremaine, S., Richstone, D., et al. 1998, *AJ*, 115, 2285
- Murray, N., Quataert, E., & Thompson, T. A. 2005, *ApJ*, 618, 569
- Mutchler, M., Bond, H. E., Christian, C. A., et al. 2007, *PASP*, 119, 1
- Nagao, T., Maiolino, R., Marconi, A., et al. 2011, *A&A*, 526, A149
- Noterdaeme, P., Laursen, P., Petitjean, P., et al. 2012, *A&A*, 540, A63
- Ohyama, Y., Taniguchi, Y., Iye, M., et al. 2002, *PASJ*, 54, 891
- Pettini, M., Shapley, A. E., Steidel, C. C., et al. 2001, *ApJ*, 554, 981
- Pilbratt, G. L., Riedinger, J. R., Passvogel, T., et al. 2010, *A&A*, 518, L1
- Poglitsch, A., Waelkens, C., Geis, N., et al. 2010, *A&A*, 518, L2
- Roussel, H., Wilson, C. D., Vigroux, L., et al. 2010, *A&A*, 518, L66
- Rubin, R. H., Simpson, J. P., Erickson, E. F., et al. 1988, *ApJ*, 327, 377
- Rubin, R. H., Dufour, R. J., & Walter, D. K. 1993, *ApJ*, 413, 242
- Rupke, D. S., & Veilleux, S. 2011, *ApJ*, 729, 27
- Rupke, D. S., Veilleux, S., & Sanders, D. B. 2005a, *ApJS*, 160, 87
- Rupke, D. S., Veilleux, S., & Sanders, D. B. 2005b, *ApJS*, 160, 115
- Rupke, D. S., Veilleux, S., & Sanders, D. B. 2005c, *ApJ*, 632, 715
- Sequist, E. R., & Clark, J. 2001, *ApJ*, 552, 133
- Schruba, A., Leroy, A. K., Walter, F., et al. 2010, *ApJ*, 722, 1699
- Shapley, A. E., Steidel, C. C., Pettini, M., et al. 2003, *ApJ*, 588, 65
- Shopbell, P. L., & Bland-Hawthorn, J. 1998, *ApJ*, 493, 129
- Springel, V., Di Matteo, T., & Hernquist, L. 2005, *MNRAS*, 361, 776
- Stacey, G. J., Hailey-Dunsheath, S., Ferkinhoff, C., et al. 2010, *ApJ*, 724, 957
- Steidel, C. C., Erb, D. K., Shapley, A. E., et al. 2010, *ApJ*, 717, 289
- Strickland, D. K., & Heckman, T. M. 2007, *ApJ*, 658, 258
- Sturm, E., Verma, A., Graciá-Carpio, J., et al. 2010, *A&A*, 518, L36
- Sturm, E., González-Alfonso, E., Veilleux, S., et al. 2011, *ApJ*, 733, L16
- Tielens, A. G. G. M., & Hollenbach, D., 1985 *ApJ*, 291, 722
- Tremaine et al., Gebhardt, K., Bender, R., et al. 2002, *ApJ*, 574, 740
- Veilleux, S., Cecil, G., & Bland-Hawthorn, J. 2005, *ARA&A*, 43, 769
- Veilleux, S., Rupke, D. S. N., & Swaters, R. 2009, *ApJ*, 700, L149
- Wagg, J., Carilli, C. L., Wilner, D. J., et al. 2010, *A&A*, 519, L1
- Walter, F., Weiß, A., & Scoville, N. 2002, *ApJ*, 580, L21
- Weiß, A., Walter, F., & Scoville, N. Z. 2005, *A&A*, 438, 533
- Weiß, A., Walter, F., Downes, D., et al. 2012, *ApJ*, 753, 102
- Westmoquette, M. S., Smith, L. J., Gallagher, J. S., et al. 2009a, *ApJ*, 696, 192
- Westmoquette, M. S., Gallagher, J. S., Smith, L. J., et al. 2009b, *ApJ*, 706, 157
- Yoshida, Z., Kawabata, K. S., & Ohyama Y. 2011, *PASJ*, 63, S493
- Yun, M. S., Ho, P. T. P., & Lo, K. Y. 1994, *Nature*, 372, 530

Appendix A

We have seen in Sect. 4.2 that we find a significant difference in the morphology of the gas density map obtained using as input to the PDR modeling the datasets with the two [OI] lines (Fig. 15), and this difference is independent on the correction we apply to the observed [CII] emission due to the contribution from ionized gas. If this difference were caused by the fact that [OI] at $63\ \mu\text{m}$ is thick in these regions, we would expect to observe less [OI] $63\ \mu\text{m}$ than what is predicted by the solution obtained using the [OI] line at $145\ \mu\text{m}$, which is optically thin. We have checked this and we find the opposite answer, that is in order to make the two density map solutions similar, we should *reduce* the input flux at $63\ \mu\text{m}$. In other words, it looks like, in these regions we have too much [OI] $63\ \mu\text{m}$ flux. Although this could be related to the uncertainties of the geometrical factor equal to two we have applied to the observed [OI] $63\ \mu\text{m}$ line flux (see Sect. 4.1.2), we wanted to check whether this difference could arise from our processing steps.

Each set of input values to the PDR modeling were obtained from maps (either [CII], FIR and [OI] at $63\ \mu\text{m}$ or [CII], FIR and [OI] at $145\ \mu\text{m}$), rebinned to the largest pixel size ($6''$, that in the red channel), smoothed to the worse resolution (that of the [CII] map), reduced to the same size and aligned to the [CII] peak. In this chain of processing, the map which suffers the heaviest manipulation is that at $63\ \mu\text{m}$. This is because the original pixel size is smaller, and its PSF differs from that at $158\ \mu\text{m}$ much more than that at $145\ \mu\text{m}$. Moreover, the observations at 158 and $145\ \mu\text{m}$ were carried out in the same AOR, therefore the pointing accuracy is likely to affect these two observations in a similar way. This may give rise to alignment problems between the final map at $63\ \mu\text{m}$ and those at higher wavelengths.

For these reasons we decided to run the models again, this time using the [OI] $63\ \mu\text{m}$ map aligned on the [CII] map on the steep gradient of the flux distribution rather than to the peak (shift of $1\ \text{pixel} = 6''$). Figure A.1 clearly shows that now both gas density maps show an enhancement toward the north part of the starburst, although the values are lower for the solutions obtained with the [OI] $145\ \mu\text{m}$ line than those obtained with the [OI] $63\ \mu\text{m}$ line. The maps in the other parameters, G_0 , T_{gas} and ϕ , show the same morphology as those shown in Figs. 14, 16 and 17.

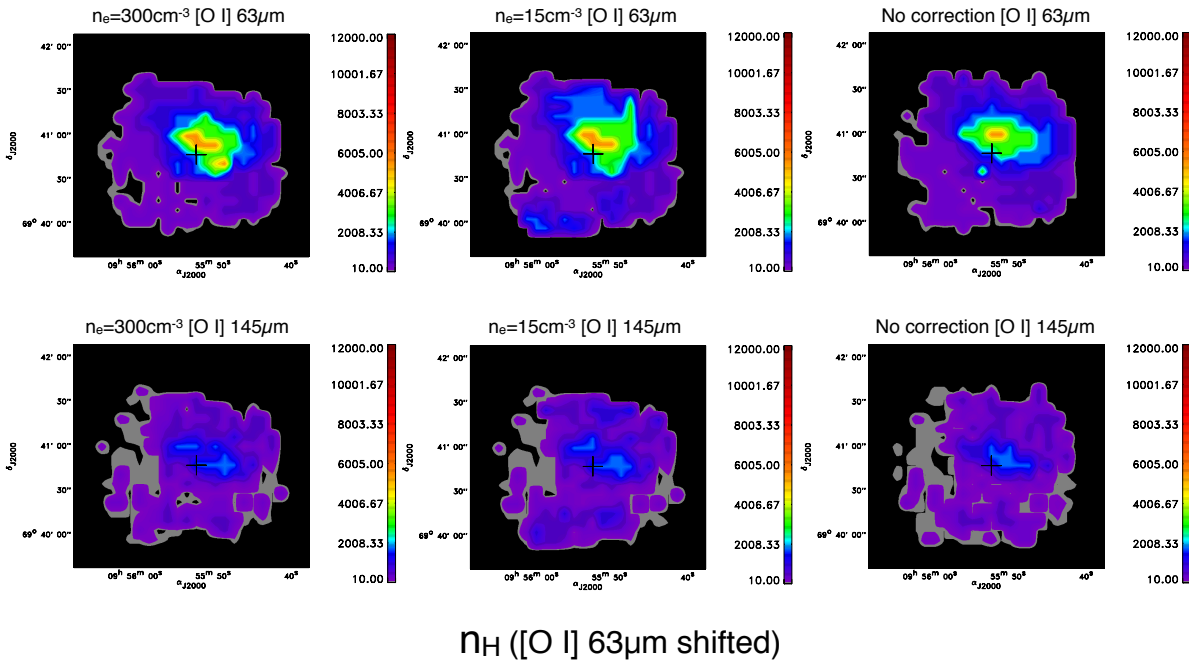


Fig. A.1. The PDR solution maps obtained for the gas density n_{H} using the [OI] map at $63\ \mu\text{m}$ shifted to match the steep gradient of the starburst region to that in the [CII] map, instead of the [CII] peak emission.